Image-based modelling for Adolescent Idiopathic Scoliosis: Mechanistic machine learning analysis and prediction

Tajdari, Mahsa; Pawar, Aishwarya; Li, Hengyang; Tajdari, F.; Maqsood, Ayesha ; Cleary, Emmett ; Saha, Sourav; Zhang, Yongjie Jessica; Sarwark, John F. ; Liu, Wing Kam

DOI
10.1016/j.cma.2020.113590

Publication date
2021

Document Version
Final published version

Published in
Computer Methods in Applied Mechanics and Engineering

Citation (APA)
Tajdari, M., Pawar, A., Li, H., Tajdari, F., Maqsood, A., Cleary, E., Saha, S., Zhang, Y. J., Sarwark, J. F., & Liu, W. K. (2021). Image-based modelling for Adolescent Idiopathic Scoliosis: Mechanistic machine learning analysis and prediction. *Computer Methods in Applied Mechanics and Engineering*, *374*, 1-30. Article 113590. https://doi.org/10.1016/j.cma.2020.113590

Available online at www.sciencedirect.com
ScienceDirect
Comput. Methods Appl. Mech. Engrg. 374 (2021) 113590
Computer methods in applied mechanics and engineering
www.elsevier.com/locate/cma

Image-based modelling for Adolescent Idiopathic Scoliosis: Mechanistic machine learning analysis and prediction

Mahsa Tajdari[a,1], Aishwarya Pawar[b,1], Hengyang Li[a,1], Farzam Tajdari[c], Ayesha Maqsood[d], Emmett Cleary[e], Sourav Saha[f], Yongjie Jessica Zhang[b,*], John F. Sarwark[d,g,**], Wing Kam Liu[a,*]

[a] *Department of Mechanical Engineering, Northwestern University, USA*
[b] *Department of Mechanical Engineering, Carnegie Mellon University, USA*
[c] *Faculty of Industrial Design Engineering, Technical University of Delft, Netherlands*
[d] *Ann & Robert H. Lurie Children's Hospital, Department of Surgery, Division of Orthopaedic Surgery & Sports Medicine, USA*
[e] *Keck School of Medicine, University of Southern California, USA*
[f] *Theoretical and Applied Mechanics, Northwestern University, USA*
[g] *Northwestern University Feinberg School of Medicine, USA*

Available online 8 December 2020

Abstract

Scoliosis, an abnormal curvature of the human spinal column, is characterized by a lateral deviation of the spine, accompanied by axial rotation of the vertebrae. Adolescent Idiopathic Scoliosis (AIS) is the most common type, affecting children between ages 8 to 18 when bone growth is at its maximum rate. We propose a mechanistic machine learning algorithm in order to study patient-specific AIS curve progression, which is associated with the bone growth and other genetic and environmental factors. Two different frameworks are used to analyse and predict curve progression, one with implementing clinical data extracted from 2D X-ray images and the other one with incorporating both clinical data and physical equations governing the non-uniform bone growth. The physical equations governing bone growth are affiliated with calculating all stress components at each region. The stress values are evaluated through a surrogate finite element simulation and a bone growth model on a detailed patient-specific geometry of the human spine. We also propose a patient-specific framework to generate the volumetric model of human spine which is partitioned into different tissues for both vertebra and intervertebral disc. It is shown that implementing physical equations governing bone growth into the prediction framework will notably improve the prediction results as compared to only using clinical data for prediction. In addition, we can predict curve progression at ages outside the range of training samples.

Keywords: Adolescent idiopathic scoliosis of the human spine; X-ray images; Patient-specific geometry; Surrogate finite element and bone growth models; Predictive models; Mechanistic machine learning

* Corresponding authors.
** Corresponding author at: Ann & Robert H. Lurie Children's Hospital, Department of Surgery, Division of Orthopaedic Surgery & Sports Medicine, USA
E-mail addresses: jessicaz@andrew.cmu.edu (Y.J. Zhang), jsarwark@luriechildrens.org (J.F. Sarwark), w-liu@northwestern.edu (W.K. Liu).
[1] Mahsa Tajdari, Aishwarya Pawar, and Hengyang Li contributed equally to this work.

https://doi.org/10.1016/j.cma.2020.113590

1. Introduction

Scoliosis, a 3D deformation of the human spinal column, is characterized by a lateral curvature of the spine, accompanied by axial rotation of the vertebrae. Adolescent Idiopathic Scoliosis (AIS) is the most common type, comprising of about 80% of paediatric scoliosis and affecting about 3% of adolescents under the age of 16. The treatment of scoliosis is highly dependent on the shape and degree of spinal curvature, and while guidelines have been established for best practices in management, individual treatment options are based on surgeon experience. Therefore, the development of a clinically-validated, patient-specific model of the spine to aid surgeons in understanding AIS in its early stages and inform optimal surgical and non-surgical treatment could provide substantial clinical value.

Curve progression in AIS is generally thought to result from multifactorial interplay of genetic and biomechanical factors. An initial curvature of unknown etiology develops, leading to varying perpendicular loads on each aspect of the vertebral bodies. Because growing bone reacts to loads applied to the growth plates, this disparity of forces causes different rates of longitudinal endochondral growth, leading to exacerbation of lateral curvature and subsequent axial rotation (the Heuter–Volkmann effect) [1].

Previous biomechanical investigations of AIS pathogenesis describe common features that could allow patient-specific predictive modelling. Curve progression was replicated in [2] using models of several pathogenesis hypotheses, and identified initial frontal plane eccentricity, with or without sagittal offset, as the prime lesion driving curve progression. In [3], geometric representations of muscle efforts were used to predict progression of lumbar scoliosis, supporting the idea that curve progression is perpetuated by asymmetries in the forces exerted by musculature. In [4], the effect of gravity, anterior spinal growth, and intervertebral disc stiffness on 3D models derived from X-ray images of normal and scoliosis patients was explored, finding that increased anterior growth produced torsion and decreased disc stiffness produced larger scoliotic deformities. A validated finite element model proposed by [5] was able to replicate the initiation of scoliosis with asymmetric stiffness of the intertransverse ligament and ligamentum flavum, suggesting that unilateral postponement of ligamentous growth may play a role in the induction of scoliosis. A physiologically-accurate finite element model of the L3–L4 vertebrae and disc of a healthy patient proposed in [6], accounting for varying densities of cortical and cancellous bone, cartilaginous endplate, annulus fibrosis, and nucleus pulposus, demonstrated vertebral wedging and asymmetric growth over three years characteristic of scoliosis.

The advent of data-driven science and artificial intelligence has driven the clinical research to unprecedented heights. The high accessibility of large processors and memory that can handle large amounts of data have made machine learning in medical applications a very promising research area of late [7,8]. Machine learning has been extensively used in the field of computer vision [9], developing prognostic models [10], and providing clinical diagnosis [11]. One such application is using deep learning (a subset of machine learning) in the prediction of AIS severity in patients. Deep learning methods have been used in automated scoliosis screening from images [12]. Machine learning has also been used to predict spinal curve progression in patients from clinical data [13–15].

Challenges in solving the AIS through modelling are (a) lack of consistent medical data for a specific person over the time, and (b) need for very fast predictive method suitable to be used by the medical practitioners. The lack of data can be compensated with detail mechanistic modelling. Here, *mechanistic* refers to the predictive physical or mathematical theories to explain a phenomenon. However, detail modelling comes at a price of and deep learning method to model the progression of spinal curvature in AIS patients. The framework presented here is a specific application of Hierarchical Deep Learning Neural Network (HiDeNN). There is a companion paper by Saha et al. [16] in the same issue which addresses the overall HiDeNN framework. Interested readers are referred to the other article for more details on the overarching vision on how high computational cost. On the other hand, deep learning models are faster but lack mechanistic interpretation and require a large amount of data. Hence, in this work the authors have tried to merge mechanistic knowledge mechanistic knowledge and data science can be combined. This article will only discuss how to implement it in the context of AIS patients' spinal curve progression.

In this paper, we propose three steps towards predictive modelling of patient-specific geometry from images:

1. Generating a patient-specific geometry of the spine from X-ray images;
2. Developing a patient-specific 3D surrogate finite element model together with a bone growth model of the spine including all different tissues of vertebra and intervertebral disc; and
3. Predicting AIS progression using mechanistic machine learning.

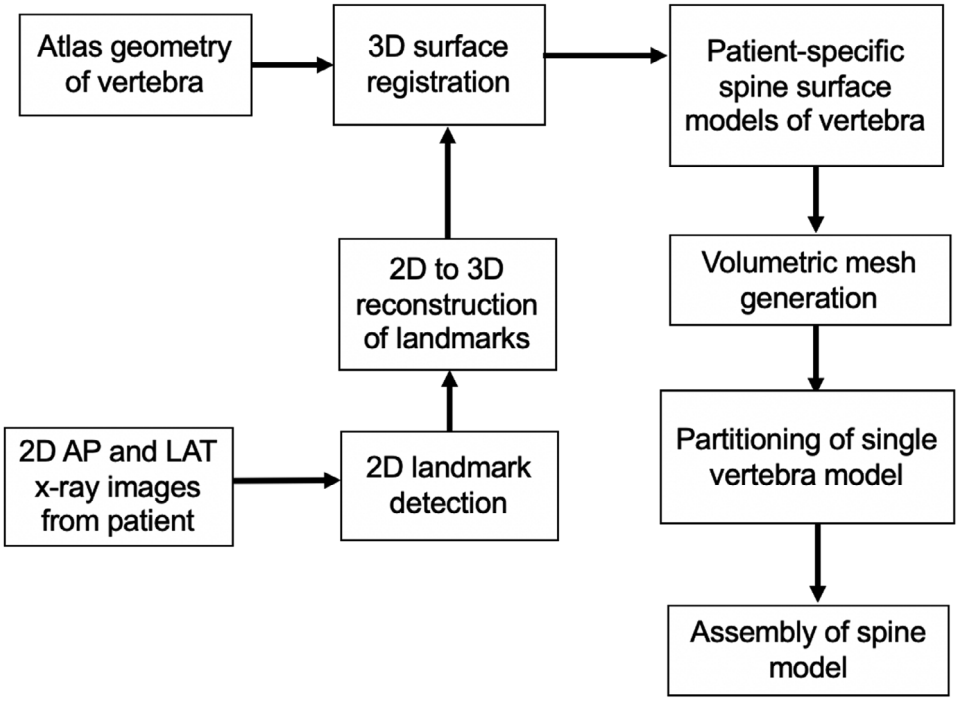

Fig. 1. The pipeline describing the framework for generating patient-specific models from X-ray images and an atlas model.

The prediction framework is designed to incorporate both clinical data obtained by the 2D X-ray images and governing physical equations of non-uniform bone growth. The proposed mechanistic machine learning framework is able to predict spine curvature outside of the range of the input trained data of the system. Access to a predictive, patient-specific model at an initial scoliosis evaluation will enable the physicians to better understand and predict curve progression, affording them better opportunities to educate families, choose among appropriate treatment options, and assess for surgical intervention.

The organization of the paper is as follows: In Section 2, we describe the framework to create the patient-specific geometry from X-ray images in detail. In Section 3, we describe the simulation of the spine model in detail, particularly the spine geometry, governing equations, material property and boundary conditions. In Section 4, the prediction of the spine curvature using mechanistic neural network is described in detail. Finally, we provide the conclusion and details on the future work in Section 5.

2. Framework for generating patient-specific spine geometry

In this section, we provide detailed explanation on the generation of patient-specific geometry [17] from X-ray images. In Fig. 1, we can see the steps carried out in the framework. Details on each step are explained. As described in the pipeline, the input to the framework are anteroposterior (AP) and lateral (LAT) 2D X-ray images and an atlas model geometry of individual vertebra. From the AP and LAT 2D X-ray images, the 2D landmarks are identified which are the corner points of each vertebra. The 2D points are then reconstructed to 3D and in the next step, we perform shape registration of the landmark points and the atlas model to generate patient-specific geometry of individual vertebra. The surface models of each vertebra are converted to volumetric mesh which is partitioned into growth plate, cortical bone and cancellous bone regions. In the last step, the final spine model is assembled from individual vertebrae.

To collect the imaging data for this project, we selected patients with AP thoracolumbar XR imaging from the radiology records of a large urban tertiary paediatric hospital (Lurie Children's in Chicago, Illinois) between September 2011 and July 2019. Demographic data was collected, along with radiographic diagnoses. Scoliotic curvature was defined as Cobb Angle $> 10^{\circ}$ [18]. Those patients with neuromuscular etiologies and structural

Table 1
Demographic information for the XR imaging data.

Features	Scoliosis	Control
Number of patients	190	163
Sex	103 Female	83 Female
Age range	2–18 years	7 months–21 years
Spinal fusion	55	0

deformities (e.g. spina bifida) were excluded. Patients were between 7 months to 21 years of age. Of those patients with radiographically diagnosed scoliosis, 190 were included with age at study ranging from 2 to 18 years. 130 of these patients were female. 55 of these patients had at least one level of operative vertebral fusion. 163 patients without radiographically diagnosed scoliosis met the inclusion criteria, ranging in age from 7 months to 21 years. Of these, 83 patients were female. None underwent spinal fusion. Demographic data is shown in Table 1.

The data-set for atlas geometry is extracted from [19], which includes a total of 86 models of lumbar vertebrae. We use a part of the dataset as the atlas geometry of the lumbar vertebrae. We have used the dataset from [20] to obtain the atlas geometry for thoracic vertebrae. As the quality of surface meshes affects volumetric meshing, all the surface meshes are re-meshed to 8000 vertices [21], resulting in uniform triangle surface meshes.

2.1. Landmark detection for 2D x-ray images

In this section, we provide a detailed explanation of the process of extracting landmarks from X-ray images in order to generate patient specific geometry (Section 2.1.1) and to study non-uniform bone growth in finite element simulation (Section 2.1.2).

2.1.1. Geometry generation landmark

In the first step, landmarks at each corner point of individual vertebra in 2D anteroposterior (AP) and lateral (LAT) X-ray images are identified. The detection of landmarks has been extensively studied in [22,23]. Here we use a semi-automatic method based on [23] to detect the corner points in the images. We first carry out image denoising using anisotropic filtering [24]. This enables noise removal in the images while at the same time highlighting the edges of the vertebra. In the next step, the centres of each vertebra are marked manually. The initial contour is created around each centre and active contour model based on gradient vector flow (GVF) snakes [25,26] is introduced, where the active contours evolve around each vertebra. Here, each contour is initialized as a rectangle with 16 landmark points for each vertebra in the AP and LAT X-ray images. We choose these landmarks to ensure that we can get accurate 3D reconstruction of the overall shape of each vertebra. Image segmentation of each vertebra is carried out, providing the final positions of the 2D landmark points as can be seen in Fig. 2. 3D reconstruction of the 2D landmark points from AP and LAT X-ray images is carried out based on [27]. The final landmark points in 3D are obtained for each vertebra and in the next step surface registration is carried out to generate patient-specific spine geometry.

2.1.2. Bone growth landmarks

In order to track non-uniform bone growth, we extract landmarks from X-ray images. Ideally, the landmarks should be on the top and bottom surface of each vertebra corresponding to growth plate to track the non-uniform bone growth of the non-planar surface. Here, the 4 corners of each vertebra from a AP and LAT X-ray images are used to model bone growth. As seen in Fig. 3(a), the 4 corners of each vertebra are extracted from X-ray images. These corner points are reconstructed in 3D to correspond to top (Fig. 3(b)) and bottom (Fig. 3(c)) regions of the growth plates of each vertebra and are chosen so that we can get a good representation of the bone growth region. By performing finite element simulation, these landmarks are tracked by the finite element mesh to account for the non-uniform bone growth.

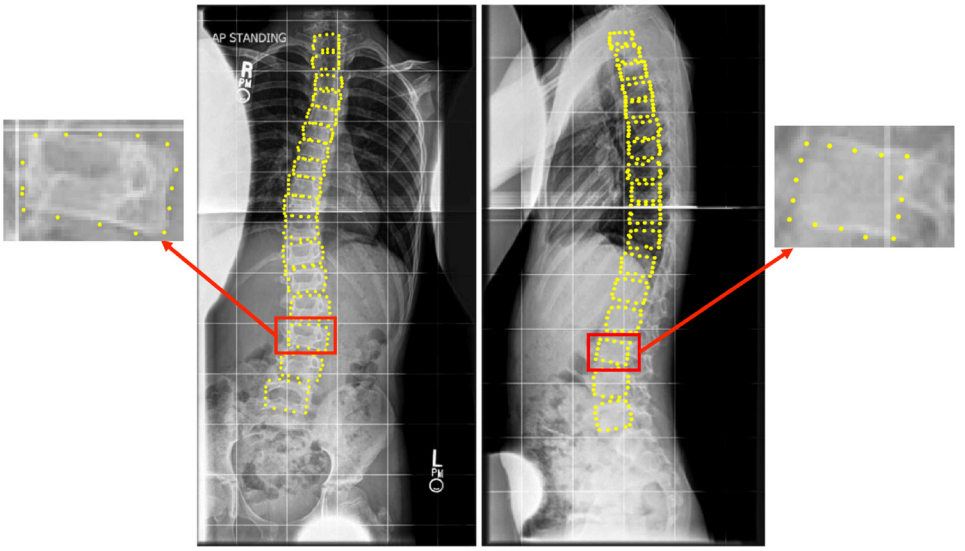

Fig. 2. Identification of landmarks (yellow dots) for the lumbar and thoracic vertebrae from AP (left) and LAT (right) X-ray images. The close-up views of the landmark points for the L3 vertebra are shown for both images. (For interpretation of the references to colour in this figure legend, the reader is referred to the web version of this article.)

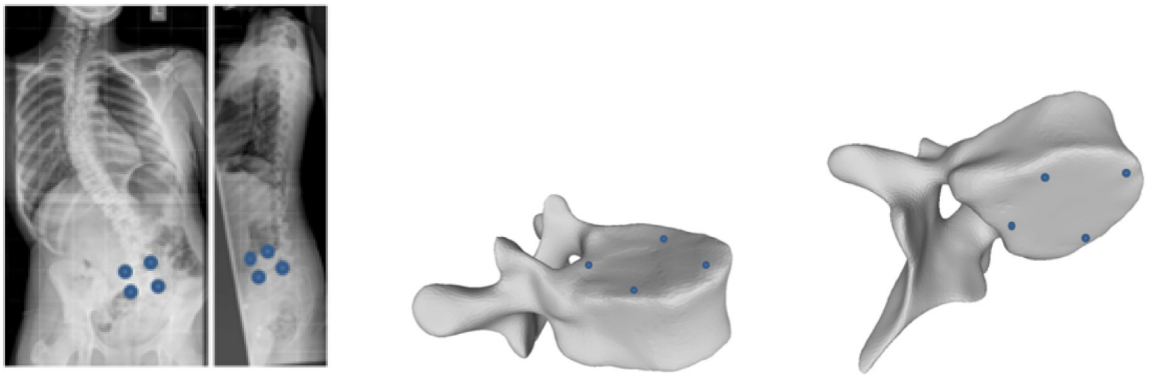

(a) (b) (c)

Fig. 3. Identification of landmarks (blue dots) for *L5* from AP and LAT X-ray images (a). The close-up views of the registered landmark points for the *L3* vertebra are shown for both top (b) and bottom (c) surfaces. (For interpretation of the references to colour in this figure legend, the reader is referred to the web version of this article.)

2.2. Generating patient-specific geometry using surface registration

In Section 2.1, the 3D landmark points obtained through reconstruction are defined as the target geometry in surface registration. The atlas models are used as the source geometry during registration. Our objective is to find a transformation function that aligns the source geometry to match with the target geometry.

We first carry out rigid alignment to align the source and target geometry. Next, to perform non-rigid surface registration, we use an incremental free form deformation based framework with iterative closest point algorithm based on the approach given in [28]. At each iteration, we define an implicit representation using signed distance function as given in [29]. The resulting smooth and continuous deformation field based on B-splines, controls the evolving shape of the source geometry. We also use coarse-to-fine strategy given in [28] to increase the accuracy

and efficiency of the registration framework. The deformation field $y(\mathbf{x})$ is defined as

$$y(\mathbf{x}) = \sum_{m=1}^{N_b} \mathbf{C}_m B_m(\mathbf{x}), \tag{1}$$

where $\mathbf{C}_m$ are the set of control points associated with the trivariate B-spline basis functions $B_m(\mathbf{x})$. N_b represents the total number of basis functions with n_1, n_2 and n_3 as the number of basis functions in each parametric direction. $B_m(\mathbf{x})$ is the tensor product of pth order univariate B-spline basis functions $N_{i,p}(u)$, $N_{j,p}(v)$ and $N_{k,p}(w)$ defined on the open knot vectors $U = \{u_1, \ldots, u_{n_1+p+1}\}$, $V = \{v_1, \ldots, v_{n_2+p+1}\}$ and $W = \{w_1, \ldots, w_{n_3+p+1}\}$ spanning the 3D space in u, v and w directions, respectively. We calculate $y(\mathbf{x})$ based on the variational formulation proposed in [30] where in each iteration we minimize the mean squared error (MSE) between the implicit representation of the evolving source and fixed target geometry. The energy functional is defined as

$$\begin{aligned} E(y(\mathbf{x})) \quad &= \int_{\Omega} (\phi_s(y(\mathbf{x})) - \phi_t(\mathbf{x}))^2 \, \mathrm{d}\Omega \\ &+\lambda_1 \int_{\Omega} \left(\|y_{,u}(\mathbf{x})\|_2^2 + \|y_{,v}(\mathbf{x})\|_2^2 \; + \|y_{,w}(\mathbf{x})\|_2^2 \right) \mathrm{d}\Omega \\ &+\lambda_2 \int_{\Omega} \left(\|y_{,u}(\mathbf{x})\|_2^2 \|y_{,v}(\mathbf{x})\|_2^2 - (\langle y_{,u}(\mathbf{x}), y_{,v}(\mathbf{x}) \rangle)^2 \right) \\ &+(\|y_{,v}(\mathbf{x})\|_2^2 \|y_{,w}(\mathbf{x})\|_2^2 - (\langle y_{,v}(\mathbf{x}), y_{,w}(\mathbf{x}) \rangle)^2) \\ &+(\|y_{,u}(\mathbf{x})\|_2^2 \|y_{,w}(\mathbf{x})\|_2^2 - (\langle y_{,u}(\mathbf{x}), y_{,w}(\mathbf{x}) \rangle)^2) \, \mathrm{d}\Omega, \end{aligned} \tag{2}$$

where λ_1 and λ_2 are two regularization parameters for the first and second order regularization [30,31]. We set λ_1 and λ_2 to 0.0001 during the entire registration process. $y_{,u}(\mathbf{x})$, $y_{,v}(\mathbf{x})$ and $y_{,w}(\mathbf{x})$ are the first derivatives of $y(\mathbf{x})$ with respect to u, v and w, respectively. The minimization of the energy functional with respect to the control points is carried out as given in [30].

The detailed algorithm for the 3D landmark based surface registration is given in Algorithm 1. The iterative loop is terminated only when MSE reaches below a certain pre-defined threshold value ($\bigtriangledown$) or when the maximum iteration number is reached. The L3 vertebra model before and after registration is shown in Fig. 4. Surface registration is carried out for all the vertebrae and the final surface geometry of the spine is assembled.

Algorithm 1: Description of the 3D landmark based surface registration

Input : Source (atlas) geometry with vertices $\mathbf{P}_s$ and target geometry with vertices $\mathbf{P}_t$. $\mathbf{C}^0$ are the initialized B-spline control points for the deformation field such that $y(\mathbf{x}) = \sum_{m=1}^{N_b} \mathbf{C}_m^0 B_m(\mathbf{x}) = \mathbf{x}$. Initial number of control points is set to N_b and $\mathbf{P'}_s = \mathbf{P}_s$.

Output: Registered atlas geometry with vertices $\mathbf{P'}_s$ such that $\mathbf{P'}_s \approx \mathbf{P}_t$.

1 **while** MSE $> \Delta$ *OR* $i <$ MAXITER **do**

1. $N_b = N_b + 1$.
2. Initialize the B-spline control point lattice ($\mathbf{C}^0$) of size N_b.
3. For each point in the source geometry $\mathbf{P'}_s$ the closest point is chosen in the target geometry $\mathbf{P}_t$.
4. Define the implicit representation of the evolving source geometry $\mathbf{P'}_s$ and target geometry $\mathbf{P}_t$ as $\phi_s(\mathbf{x})$ and $\phi_t(\mathbf{x})$ using distance function.
5. Evaluate the deformation field $y(\mathbf{x})$ using updated control points $\mathbf{C}$ through minimization of the energy functional.
6. Based on $y(\mathbf{x})$, the new vertex positions of the source geometry $\mathbf{P'}_s$ are computed.

2 **end**

2.3. Generating volumetric meshes for finite element simulation

We generate 3D finite element mesh of the spine from the patient-specific surface meshes which are obtained by using surface registration. The finite element model of the spine consists of three components: intervertebral discs, lumbar vertebrae and thoracic vertebrae. The volumetric mesh of each vertebra is then segmented into growth plate,

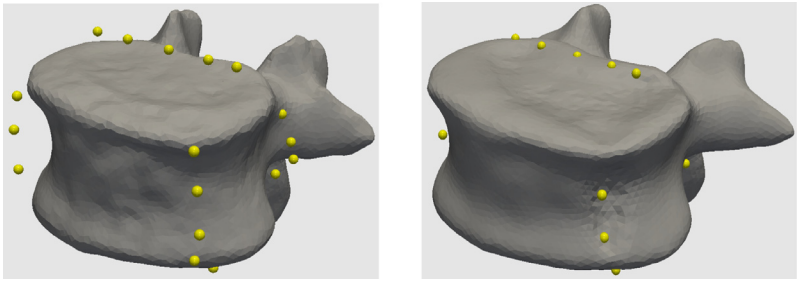

(a) (b)

Fig. 4. Generation of patient-specific geometry using landmark-based surface registration: The L3 vertebra model of the atlas geometry (a) before and (b) after registration along with the landmark points (yellow) is shown. (For interpretation of the references to colour in this figure legend, the reader is referred to the web version of this article.)

cortical bone and cancellous bone regions. Similarly, the volumetric mesh of each intervertebral disc is partitioned into Annulus Fibrosus and Nucleus Pulposus regions.

The volumetric meshes of lumbar vertebrae, thoracic vertebrae and intervertebral discs are generated as follows. We first generate the surface mesh of the intervertebral disc. The intervertebral disc fills the gap between two adjacent vertebrae. The contact points of disc with each vertebra are automatically generated by registering a source surface mesh with manually defined the contact points. L3 and T8 vertebrae are selected as the source meshes for lumbar and thoracic vertebrae, respectively. The contact points of each vertebra with bottom disc (green), and top disc (red) are shown in Fig. 5. Then, a mesh consisting of the bottom surface of each vertebra and the top surface of the adjacent vertebra (for e.g., T1 bottom surface with T2 top surface) is extracted and uniformly re-meshed [21]. The uniform mesh size is extracted by numerically minimizing a cost function [32] including a mesh size term, the number of meshes, and differences between each mesh size field of a simulation mesh model and the initial mesh size field as discussed in Appendix A. The results of solving the optimal problem for each vertebrae are summarized in Table 13 in terms of number of elements and size of mesh. Then, the contact points of the intervertebral disc are replaced with the extracted mesh. The generated lumbar intervertebral disc between L1 and L2 vertebrae is shown in Fig. 6.

In order to segment each component, a second surface is generated by moving along the normal vector on each vertex of the surface. Then, the intersecting faces (and vertices) are detected and deleted. In the last step, the original surface is registered to the new surface and the inner region is extracted. An external 3D mesh generator [33] is used to create tetrahedral meshes from the closed surface meshes. It implements a fast mesh-based Monte Carlo (MC) photon migration algorithm for static and time-resolved imaging in 3D complex media.

3. Surrogate finite element spine model

In this section, a surrogate spine model is developed to approximate the selected properties based on the results of the physical model. A surrogate model is the one that approximates a more complex, higher fidelity model and can be used in place of the said complex model [34]. Surrogate modelling is a well-known approach to study various industrial engineering problems and is a great tool to assist the computationally expensive analysis and optimization [35]. In this research, a surrogate spine model is introduced in which the modelling parameters are fitted to get the best result. Previous efforts on building spine models are found in [36], where the models are validated for single distinct spinal geometry with one set of material properties. This fact raises the question regarding the validity of the results and compatibility with the *in vitro* and *in vivo* results. As presented in Appendix C, the surrogate model is validated based on the reported range of data in the literature. It should be noted that indirect validation is used as described in [37] since the *in vivo* stress distribution on each distinct geometry is not available. The results obtained by the surrogate model will be used in the Mechanistic NN (Section 4) and will provide the "trend" of the output prediction data. As explained in Section 2, the 3D finite element meshes of the vertebrae

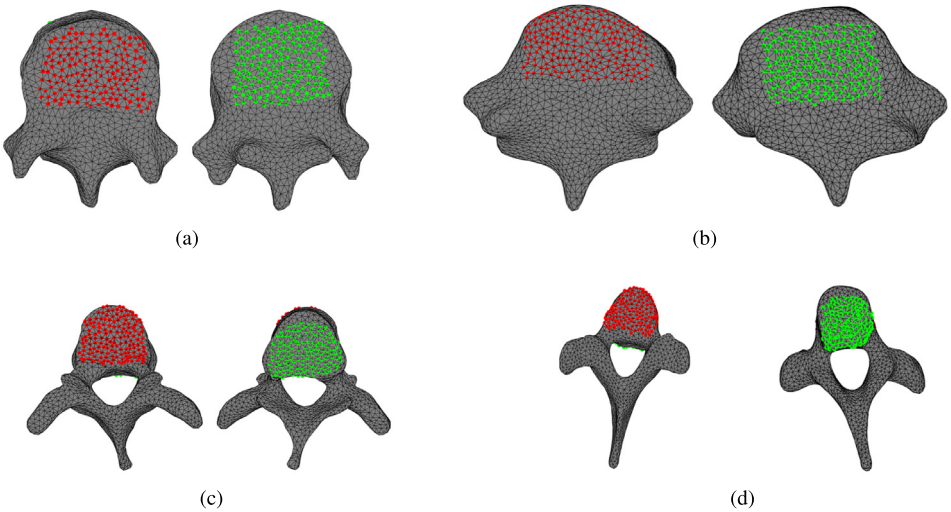

Fig. 5. Contact points of a vertebra to a disc. (a) L3 (used as reference surface for lumbar vertebra); (b) L5, (c) T8 (used as reference surface for thoracic vertebra) and (d) T1. The red dots are the contact points on the top surface and the green dots are the contact points on the bottom surface of each vertebra. (For interpretation of the references to colour in this figure legend, the reader is referred to the web version of this article.)

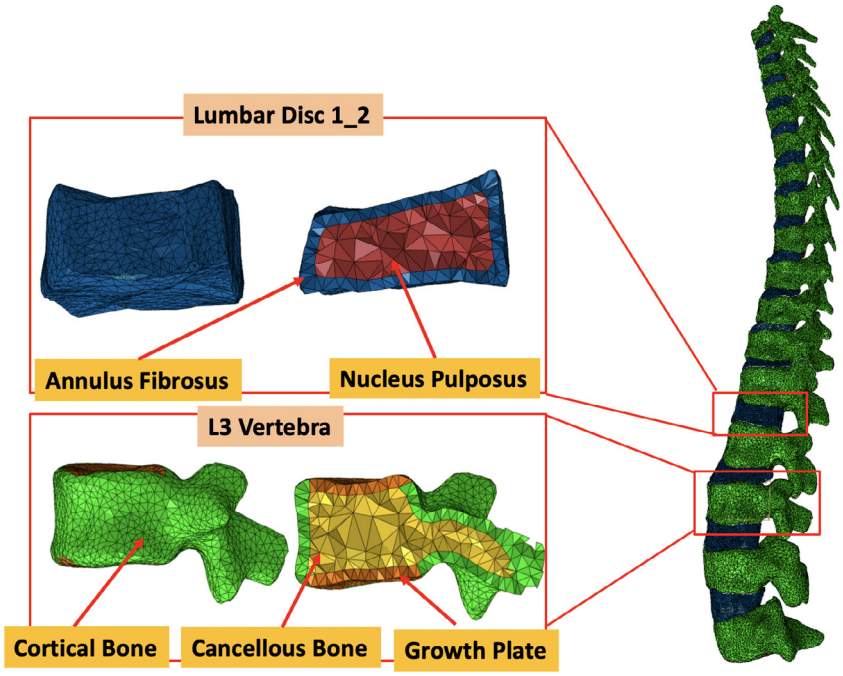

Fig. 6. The 3D finite element mesh of the spine consisting of the lumbar vertebrae, thoracic vertebrae and intervertebral discs. The close-up views are of the partitioning of a single vertebra into the growth plate at the level of the cortical bone and cancellous bone and the intervertebral disc into the Annulus Fibrosus and Nucleus Pulposus regions are shown in.

and intervertebral discs are generated using X-ray images. Each vertebra is partitioned into cortical and cancellous bone and growth plate regions and each intervertebral disc (IVD) is partitioned into annulus fibrosus and nucleus pulposus regions as shown in Fig. 6. Linear elastic material property is considered for each tissue [38] as given in Table 2 (for 39 months) and tetrahedral elements are used for the entire spine. Since AIS targets patients in early

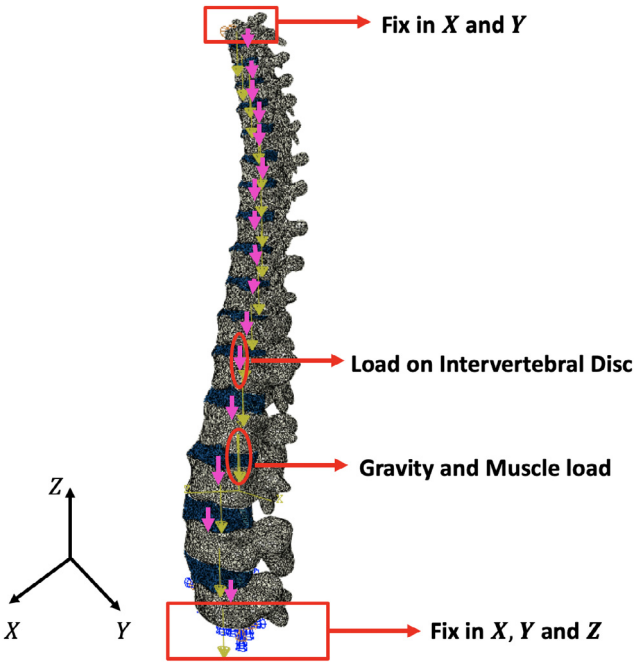

Fig. 7. Schematic representation showing the applied gravitational and muscular load on each vertebra, applied load on the intervertebral disc and the boundary conditions for the finite element simulation.

ages, published literature proposed using a constant elastic modulus before 15 years old [39]. However to be more precise, the mechanical properties of cortical bone can be updated (see Table 14 in Appendix C) for a given year before 13 years old. In this simulation, the material properties are updated accordingly for each year.

The total number of elements and vertices of the spine geometry is 595,573 and 128,205, respectively. The boundary conditions are defined such that the bottom surface of the L5 vertebra is fixed in all directions (X, Y and Z) and the top surface of the T1 vertebra is fixed to allow no motion in X and Y directions. In order to connect each intervertebral disc to the adjacent vertebrae, the nodes located on the top surface of the disc are linked to the nodes on the bottom surface of the top-adjacent vertebra. Similarly, the nodes at the bottom surface of the disc are linked to all the nodes on the top surface of the bottom-adjacent vertebra.

There are two forces applied on the spinal column. The first one is the gravitational force and the second one is the vertical stabilizing force due to the surrounding muscles of the vertebrae as it is shown in Fig. 7. The dominant direction of the resultant loads on the spinal column is presumed to be close to the direction of the gravitational force. Gravitational load is applied at the centre of mass of each vertebra and it is applied to each vertebral level unevenly based on the work proposed in [40]. In order to consider the effect of the surrounding muscles on the vertebral body in the standing position, the gravitational load increases as given by the equation $F^i = (15 + 2.1\, M_i)$ [41], where F^i is the total force applied on each vertebra v^i $(i = 1, \ldots, 17)$ and M_i is the percentage of the total mass of each vertebra as described in Table 3 for a subject with the weight of the spine given as 16.5 kg (at 39 months). The applied load on each intervertebral disc is calculated as $F_v^{(i,i-1)} = F^i - F^{(i-1)}$, where $F_v^{(i,i-1)}$ is the applied load on the intervertebral disc located between the vertebrae v^i and $v^{(i-1)}$. Based on the combination of gravitational and muscular forces that are calculated from the intervertebral disc pressure, this framework of calculating applied force on the spinal column is chosen such that it expresses the activity of the vertebral growth plates. The load applied to the spine can be dynamically updated based on the age and the weight can be estimated using [42] as described in Table 4 (see Fig. 7).

Bone Growth: Spinal column overgrowth in AIS patients is observed during puberty where bone growth is at its maximum rate [43,44]. It has been reported that AIS patients have longer spinal columns as compared to the control patients, especially within the thoracic region [45,46]. Relative anterior spinal overgrowth (RASO) during puberty is associated with the spinal curve progression observed in AIS. [47]. Different growth rates have been observed

Table 2
Material properties used in human spine simulation.

Tissue	Young's modulus (MPa)	Poisson's ratio
Cortical bone	768	0.3
Cancellous bone	400	0.3
Annulus fibrosus	8	0.45
Nucleus pulposus	2	0.49
Growth plate	50	0.4

Table 3
Numerical description of the applied load ($F^i = 15 + 2.1\,M_i$) on each vertebra for the patient at 39 months (16.5 kg). Force applied to each intervertebral disc is $F_v^{(i,i-1)} = F^i - F^{(i-1)} = 0.91$ kg.

Vertebral level	Vertebral name	Percentage of total mass	Mass (M_i) (kg)	F^i (kg)
1	T1	14.0	2.31	19.85
2	T2	16.6	2.73	20.75
3	T3	19.2	3.16	21.65
4	T4	21.8	3.59	22.53
5	T5	24.4	4.02	23.44
6	T6	27.0	4.45	24.34
7	T7	29.6	4.88	25.24
8	T8	32.2	5.31	26.15
9	T9	34.8	5.74	27.05
10	T10	37.4	6.17	27.95
11	T11	40.0	6.60	28.86
12	T12	42.6	7.02	29.74
13	L1	45.2	7.45	30.64
14	L2	47.8	7.88	31.54
15	L3	50.4	8.31	32.45
16	L4	53.0	8.74	33.35
17	L5	55.6	9.17	34.25

Table 4
Calculating weight based on age [42].

Age range	Weight calculation (kg)
$\leqslant 1$	(age in months + 9)/2
(1, 5]	2 × (age in years + 5)
(5, 14]	4 × (age in years)

between AIS and normal patients as well as among male and female patients [45,46,48]. The underlying etiology of AIS and pathomechanism of curve progression are not fully understood, in spite of the extensive research. However, some studies correlate AIS to a genetics, foot shape and family history [49,50]. So far, biomechanical modelling of bone tissue and growth has not been fully understood and has not been implemented in depth to examine the effect of abnormal growth of AIS spine [38]. A number of studies relate AIS to vertebral growth rate and it is assumed as the function of stress on the growth plates, which are located at the top and bottom surfaces of each vertebra.

Stokes' model is a simplified mathematical formulation of the Heuter–Volkmann principle [51,52]. It was developed based on the experimental work focusing on the relationship between mechanical modulation and bone growth rates in response to compressive or tensile stresses. Shi et al. [38] implemented Stoke's approach to simulate bone growth using the equation $G = G_1(1 - \beta_1\sigma)$, where G is the actual growth rate along the normal direction of each element defined locally and G_1 and β_1 are the patient specific constants. It is believed that the growth occurs along the normal direction of growth plates, governed by the local normal stress at each location. Same values of β_1 and G_1 were used for all the patients and at all the ages. However, it is not realistic to use the same constants for all ages and for all patients. In this work, von Mises stress is used to incorporate all the components of stress

Table 5
Growth parameters used to train $FFNN_{ca}$.

Growth parameters ($\boldsymbol{G^m}$)	(mm/year)	Growth parameters ($\boldsymbol{\beta}$)	(MPa^{-1})
G_1	0.1	β_1	0.2
G_2	0.1	β_2	0.2
G_3	0.8	β_3	0.5

and patient specific constants are introduced in three directions. We have

$$\begin{aligned} G_1 &= G_1^m(1-\beta_1\bar{\sigma}),\\ G_2 &= G_2^m(1-\beta_2\bar{\sigma}),\\ G_3 &= G_3^m(1-\beta_3\bar{\sigma}). \end{aligned} \tag{3}$$

$\boldsymbol{G} = [G_1, G_2, G_3]$ are the actual growth rates along the three normal directions (in the global coordinate system) at each surface of the element accounting for non-uniform growth. Normal growth parameters $\boldsymbol{G^m} = [G_1^m, G_2^m, G_3^m]$ (growth rate for non-scoliotic spine) and patient specific parameters $\boldsymbol{\beta} = [\beta_1, \beta_2, \beta_3]$ are the growth model parameters. In this paper, $\boldsymbol{G^m}$ is set to $= [0.1, 0.1, 0.8]$ mm/year and $\boldsymbol{\beta}$ is set to $[0.2, 0.2, 0.5]$ MPa^{-1} [38] as described in Table 5. The stress $\bar{\sigma}$ is the applied von Mises stress calculated at each landmark using the finite element model. For a long span of time, for example five years, there are both longitudinal and lateral growth in vertebra.

As seen in Fig. 8, vertebral bone has both longitudinal and lateral growth. To study the non-uniform local growth of each element, a local coordinate system is defined at each face of the tetrahedral element in which the local coordinates for one face are defined as shown in Fig. 9. The local x and y directions are the principal axes attached to each face of the elements and the local z direction is along the normal vector of the face. The origin of the local coordinate system is located at the centroid of each face. It should be noted that the corresponding elements of the surface meshes are comparable, as we are registering the volumetric mesh shown in Fig. 6 with any new surface meshes of the vertebrae extracted from the method given in Section 2.2. Thus, the number of elements and their ID numbers are the same for all the spine models. The z direction is calculated for the same element at three different time frames (68, 84 and 100 months). As shown in Fig. 9, the z direction changes at every time frame. Thus, it can be concluded that the local z direction of the surface is changing at each time frame and the bone tissue grows non-uniformly. Since bone growth is a complex problem and is not the only factor controlling AIS, in Section 4 a neural network will be designed which uses both clinical and synthetic (finite element simulation) data.

4. Prediction of the spine shape using a mechanistic neural network

In this section, we extend the study to develop predictive models for spine growth. Many approaches in the study of spine growth have been proposed that either use empirical equations or the direct application of data science. Empirical equations focus on generalizing the physical relationship between growth stress and strain. They predict growth stress and strain using underlying hypothesis that the spine growth is related to the stress applied to the growth plates. Although these equations are easy to implement, they do not consider variability of growth from patient to patient. Direct data science methods are aimed to predict the spine shape with regression methods. However, due to the presence of noise in big-data, pure data science approaches can sometimes fail to provide accurate predictions. In this section, we will introduce two neural networks. *Clinical NN* is described in Section 4.1, which implements pure data science for the prediction of curve progression from clinical image data using a feed forward neural network.

Later, in Section 4.2, we will propose a mechanistic deep learning framework (*Mechanistic NN*) considering the combination of mechanistic model, empirical equations and clinical image data to make real-time predictions of spine curvatures of AIS patients. This framework can provide real-time growth prediction for a specific patient's spine, or even predict outside the database range, which will be useful for calibration and treatment planning. The predictive capability of the mechanistic machine learning model comes from the combination of three important concepts: the kinematics and kinetics information of the landmarks from the surrogate finite element model of the spine; the bone growth model that accounts for the nonuniform bone growth; and the calibration of the clinical landmarks data from the X-ray images. In AIS research there is always a challenge of the limitation of data since

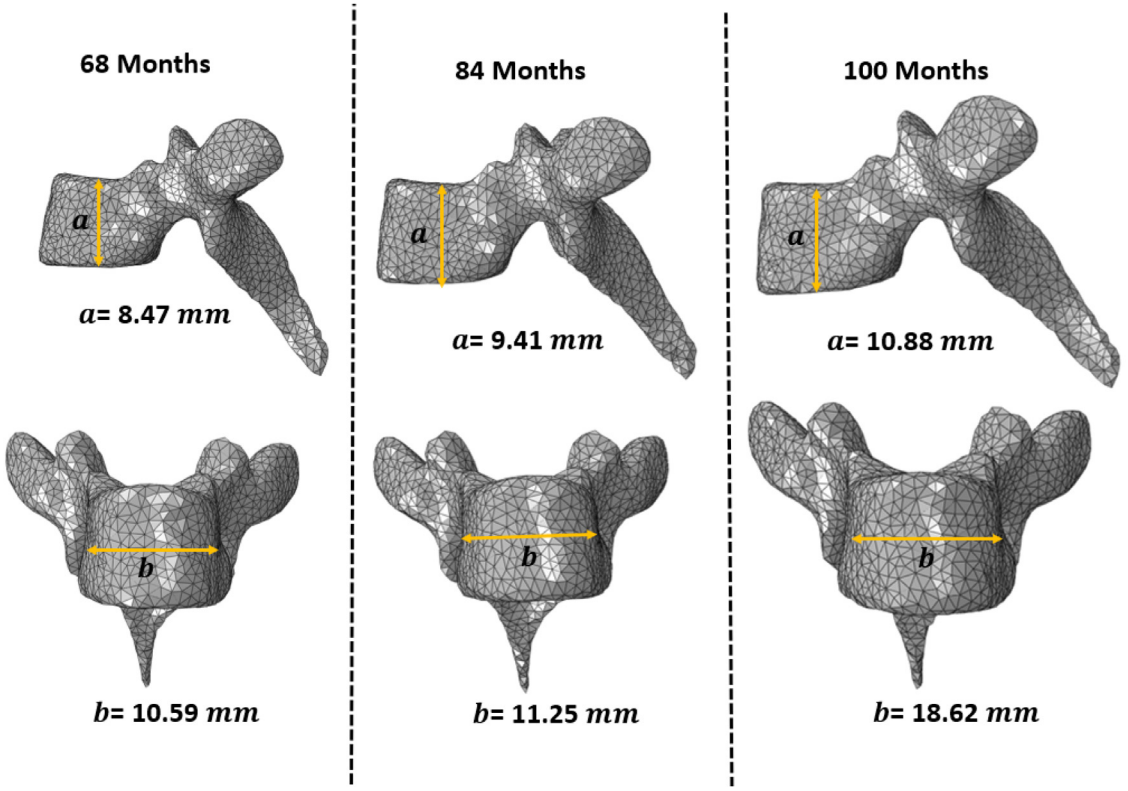

Fig. 8. Longitudinal (a) and lateral (b) vertebral growth at 68, 84 and 100 months. The top and bottom rows show the side and front views of the volumetric meshes of vertebra, respectively.

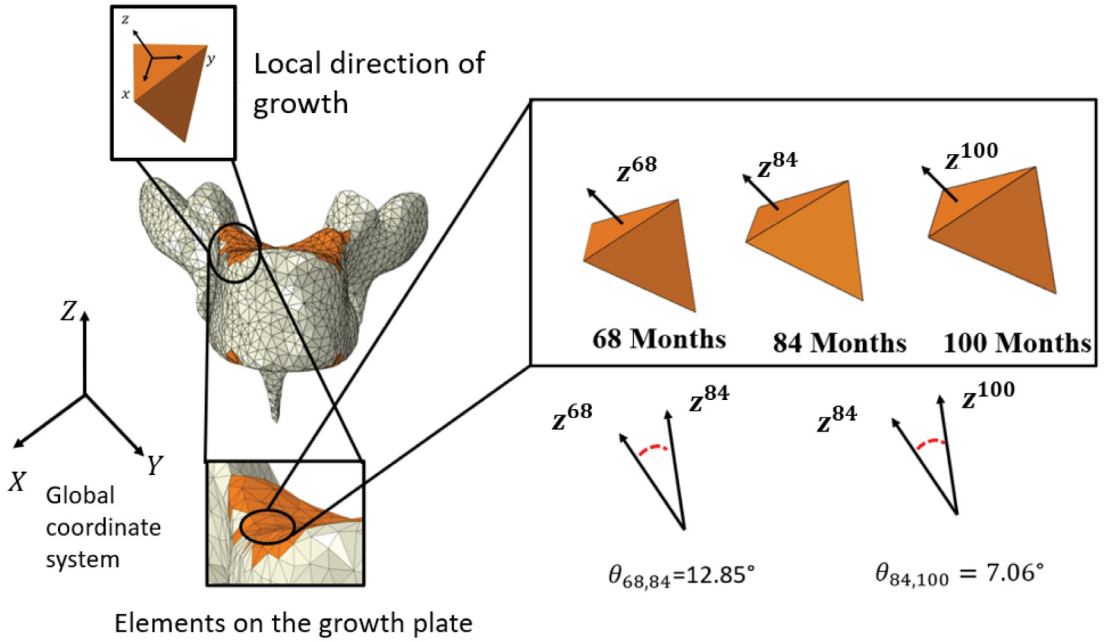

Fig. 9. Three directions of growth are shown for one element of the volumetric mesh of a vertebra. Changes in the surface normal direction are observed between 68 and 84 months and between 84 and 100 months.

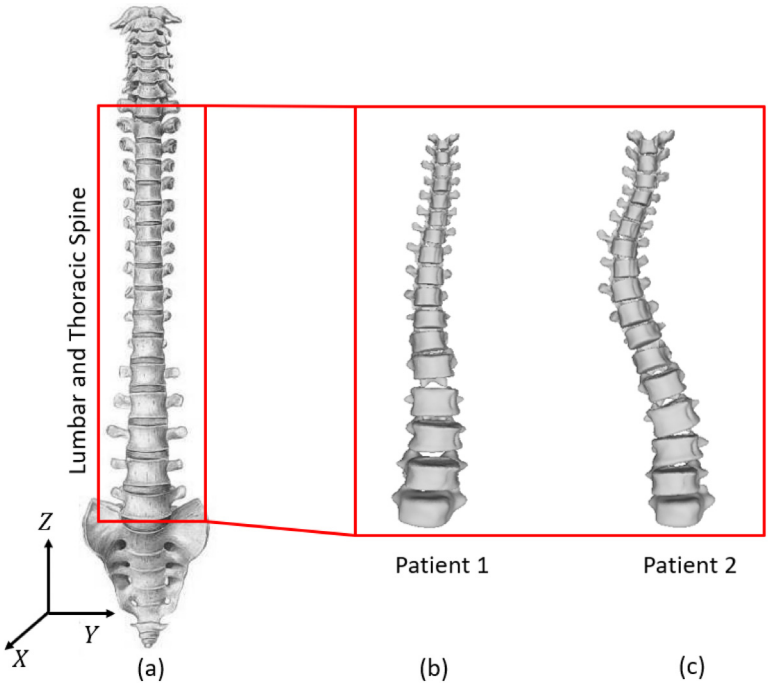

Fig. 10. The anteroposterior view of the initial geometry of (a) patient with normal curvature [54]. (b) Patient 1 with single curvature in the thoracic part and (c) Patient 2 with double curvature in thoracic and lumbar regions.

as it is explained in [53] the patient cannot be exposed to X-ray frequently. The surrogate finite element model is used to extract the kinematics and kinetics governing the motion of the landmarks in the model. Implementing the surrogate finite element model can provide the trend of the output data and circumvent the need to provide more clinical data. Moreover, it can predict outside of the range of the trained data as opposed to the traditional machine learning algorithm.

4.1. Prediction using clinical data

Data collection: The database is built from clinical X-ray images. For a patient, we consider an X-ray image at an initial stage (age t_0 months) as a reference and X-ray images at different subsequent stages of scoliosis. In our study, we use data of two patients, including nine and eight X-ray images for the first and second patient, respectively. As shown in Fig. 10(a), the normal spine does not have any curvature in the YZ plane. The lumbar and thoracic regions of the spine for these two patients used in this study are shown in Fig. 10(b) and (c), respectively. Patient 1 has a single curvature in the thoracic region and Patient 2 has double curvature, one in the thoracic region and one in the lumbar region.

For Patient 1, the initial X-ray image of the patient is taken at $t_0 = 39$ months. The subsequent six X-ray images are taken at $t = \{66, 100, 115, 118, 120, 123\}$ months, which are used for training the neural network. The remaining three X-ray images taken at $t = \{68, 84, 127\}$ months are used for comparing with the results obtained from the neural network. Each X-ray image shows the shape of spine at a certain age of the patient. This can be seen in Table 6. The same NN is used for all the 204 landmarks.

Feature selection: In order to describe the position of the vertebra, we define 12 landmark points on each vertebra, as shown in Fig. 11. A single spine has 17 vertebrae. Thus, there will be 204 landmark points for each spine. We also define 5 global angles to describe the global curvature of the spine (see Appendix B for details). Therefore, for one X-ray image at age t, we have a set of data $\boldsymbol{S}(t) = [\boldsymbol{P}^t, \boldsymbol{\alpha}^t]$, where $\boldsymbol{P}^t$ are the coordinates of 204 landmarks and $\boldsymbol{\alpha}^t$ are five global angles. We define a nonlinear mapping $\mathscr{F}(t)$ that can predict the set of data describing spine

Table 6
Data collection for the clinical neural network for Patient 1.

Identification of X-ray images	Age (months)
Initial X-ray image	39
Training X-ray images	{66, 100, 115, 118, 120, 123}
X-ray images for comparing with results from NN	{68, 84, 127}

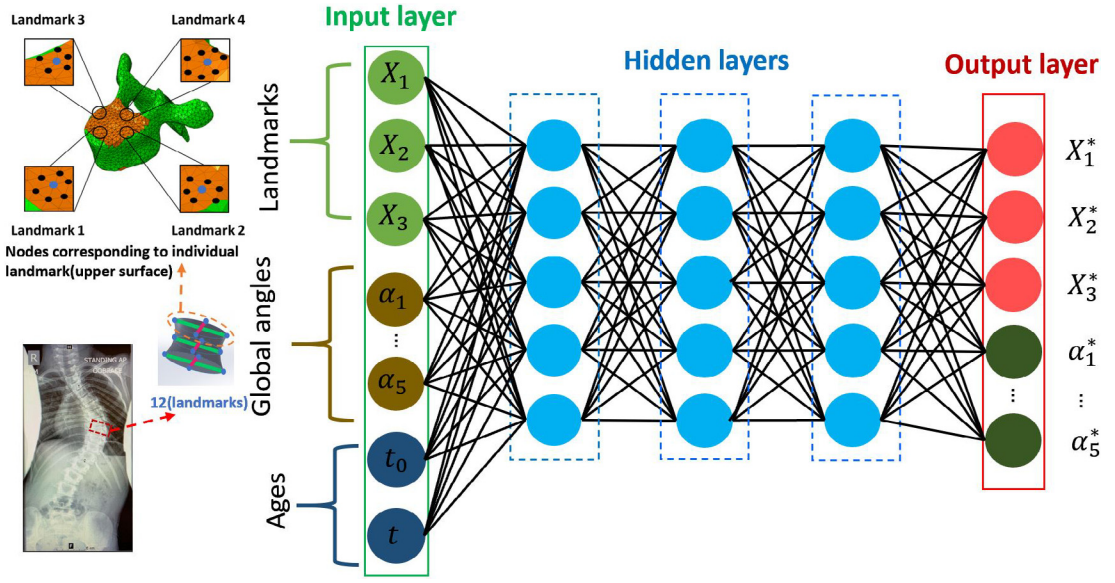

Fig. 11. Developing growth model using a feed forward neural network (FFNN_{cl}). The inputs are positions of landmarks, global angles and age. The outputs are positions of landmarks and global angles on predicted models. The total number of landmarks is: $12\,(landmarks) \times 17\,(vertebrae) \times 6\,(ages) = 1224$.

shape at age t: $\mathscr{F}(t) = [\boldsymbol{P}^t, \boldsymbol{\alpha}^t]$. Since the output of this function is a very high dimensional vector, we change the coordinates of all the 204 landmarks $\boldsymbol{P}^t$ to the coordinates of one landmark $\boldsymbol{X}^t$. We add the landmarks' initial coordinates (at $t = t_0$) into the input. The nonlinear mapping becomes $[\boldsymbol{X}^t, \boldsymbol{\alpha}^t] = \mathscr{F}(t, \boldsymbol{X}^{t=t_0})$. The initial values of five global angles also affect the training results. They are added in the input: $\mathscr{F}(t, \boldsymbol{X}^{t=t_0}, \boldsymbol{\alpha}^{t=t_0}) = [\boldsymbol{X}^t, \boldsymbol{\alpha}^t]$. We put t_0 into the input and define $\boldsymbol{X}^t = \boldsymbol{X}^*$, $\boldsymbol{\alpha}^t = \boldsymbol{\alpha}^*$, $\boldsymbol{X}^{t=t_0} = \boldsymbol{X}$. The mapping becomes $\mathscr{F}(t, t_0, \boldsymbol{X}, \boldsymbol{\alpha}) = [\boldsymbol{X}^*, \boldsymbol{\alpha}^*]$.

There are **ten** input features: **three** initial positions of a landmark $\boldsymbol{X} = [X_1, X_2, X_3]$, **five** global angles $\boldsymbol{\alpha} = [\alpha_1, \alpha_2, \alpha_3, \alpha_4, \alpha_5]$, **initial age** of the patient t_0 and **current age** of the patient t. There are **eight** output features: **three** predicted positions of a landmark $\boldsymbol{X}^*$, **five** predicted global angles $\boldsymbol{\alpha}^*$.

Clinical neural network: A neural network is built to train the relationship between the input and output variables. We use data from six X-ray images to train the neural network. In order to avoid overfitting, 15% of landmarks are used for validation and 15% of landmarks are used for testing. Therefore, the total number of landmark points used for training, testing and validation is 856, 184, and 184, respectively. The overall structure of the feed forward neural network (FFNN_{cl}) can also be described as a mapping, i.e.:

$$\begin{aligned} \boldsymbol{O} = [X_1^*, X_2^*, X_3^*, \alpha_1^*, \alpha_2^*, \alpha_3^*, \alpha_4^*, \alpha_5^*] &= \mathscr{F}_{\text{FFNN}_{\text{cl}}}(\boldsymbol{I}), \\ where\ \boldsymbol{I} &= [X_1, X_2, X_3, \alpha_1, \alpha_2, \alpha_3, \alpha_4, \alpha_5, t_0, t]. \end{aligned} \tag{4}$$

In order to explain the training procedure more clearly, notations are presented in Table 7. The neural network setup for the following two neural networks is shown in Table 8.

In each layer of a general FFNN, each neuron takes the output value from each of the neurons in the preceding layer as inputs and gives a single output. This is repeated for each layer. The value of the jth neuron in the layer

Table 7
Notation table of variables used in the feed forward neural network.

$\boldsymbol{I}^s$	Vector of input, $s = 1, \ldots, N_T$
$\boldsymbol{O}^s$	Vector of output, $s = 1, \ldots, N_T$
s	Counting index for number of samples (training or validation, depending on context)
l	Counting index for number of layers
i	Counting index for neurons in a given layer
j	Counting index for neurons in another layer
N_T	Number of training samples
N_L	Number of layers in the neural network
$N_N(l)$	Number of neurons in layer l
W_{ij}^l	Weight connecting the ith neuron in layer $l-1$ to the jth neuron in layer l
b_j^l	Bias of the jth neuron in layer l
$a_j^{l,s}$	Neuron numerical value for jth neuron in lth layer and for sth sample
$\mathscr{A}$	Activation function
$\mathscr{F}_{FFNN}$	Feedforward neural network function

Table 8
Neural network setup for neural networks.

NN components	Clinical NN (FFNN_{cl})	Calibrating NN (FFNN_{ca})	Mechanistic NN ($\text{FFNN}_{\text{ca}} + \text{FFNN}_{\text{co}}$)
Number of training samples	856	700	856
Number of test samples	184	150	184
Validation samples	184	150	184
Hidden layers	3	1	4
Neurons in hidden layers	10	10	10
Activation function	Sigmoid function $f(x) = \frac{1}{1+e^{-x}}$		

l for the sth sample can be expressed as:

$$a_j^{l,s} = \begin{cases} I_j^s, \text{ if } l = 1 \text{ (input layer)} \\ \mathscr{A}(\sum_{i=1}^{N_N(l-1)} W_{ij}^l a_i^{l-1,s} + b_j^l), \text{ if } l \in \{2, \ldots, N_L - 1\} \text{ (hidden layers)} \\ \sum_{i=1}^{N_N(l-1)} W_{ij}^l a_i^{l-1,s} + b_j^l, \text{ if } l = N_L \text{ (output layer)} \end{cases} \tag{5}$$

where $\mathscr{A}$ is an activation function, and the final layer gives the estimated coordinates:

$$O_k^s = a_k^{N_L,s}. \tag{6}$$

During training, we use the sigmoid function [55] as the activation function. W_{ij}^l is the weight connecting the ith neuron in layer $l-1$ to the jth neuron in layer l. $a_j^{l,s}$ is neuron value for the jth neuron in the lth layer and for the sth sample. N_L is the number of layers in the neural network. $N_N(l)$ is the number of neurons in each layer of the neural network. The training procedure for an FFNN can be reformulated as an optimization problem. We define the loss function (or the cost function) as the Mean Square Error (MSE). In this problem, we use three hidden layers. In order to explain the training stage, we assume one hidden layer, and the ground truth value of output is $a_k^{*,l=3,s}$. Thus, the optimization formulation is given as:

$$\begin{aligned} &find \;\; W_{ij}^l, \; b_j^l \; to \; minimize \\ &\qquad MSE = \frac{1}{N_T} \sum_{s=1}^{N_T} \left(\boldsymbol{O}^s - \bar{\boldsymbol{O}}^s \right)^2, \\ &where \; \boldsymbol{O}^s = [X_1^*, X_2^*, X_3^*, \alpha_1^*, \alpha_2^*, \alpha_3^*, \alpha_4^*, \alpha_5^*] = \mathscr{F}_{\text{FFNN}_{\text{cl}}}(\boldsymbol{I}^s, W_{ij}^l, b_j^l), \\ &\qquad \bar{\boldsymbol{O}}^s \; is \; from \; clinical \; dataset. \end{aligned} \tag{7}$$

By finding the optimal values for W_{ij}^l, b_j^l, MSE will be reduced. Note that only training data is used in this process, hence $s = 1, 2, \ldots, N_T$, where N_T is the number of training data samples. As shown in Fig. 16, the

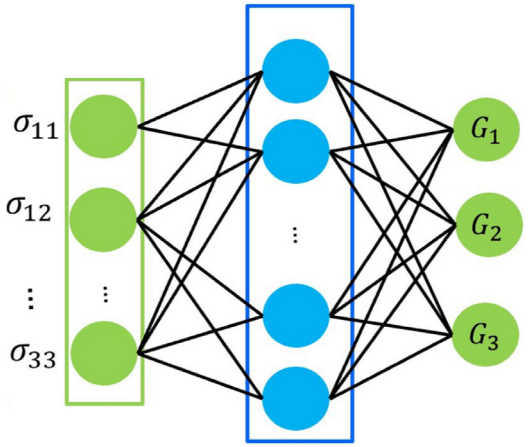

Fig. 12. FFNN_{ca} trained by data generated from physics equations. The inputs are stress components on each landmark. The outputs are growth strain components. The 1000 samples are generated by the uniform distribution within the range of possible stress values obtained from the finite element models. The stress values are evenly generated by a defined range: $\sigma_{11}, \sigma_{22}, \sigma_{33} : [-10, 10]$ MPa. $\sigma_{12}, \sigma_{21}, \sigma_{23}, \sigma_{32}, \sigma_{31}, \sigma_{13} : [-5, 5]$ MPa.

prediction of pure data science is very scattered and with low fidelity. This is due to the noisy initial data. In addition, the data also has errors in measurement or detection while evaluating the landmarks from X-ray images. Pure data science methods fail to capture the physical characteristics of spine growth. A combined clinical and mechanistic study is thus needed to investigate the scheme pertaining to bone growth.

4.2. Mechanistic neural network

As it is shown in Fig. 13, our proposed mechanistic neural network (FFNN_{m}) is a composite neural network comprising of a *calibrating* neural network (FFNN_{ca}) that tries to find a trend of growth strain from applied stress using a physics based model, and a second *correcting* neural network (FFNN_{co}) that uses the "pre-trained" growth strains as well as the previous ten features from Section 4.1 as inputs to predict the final output co-ordinates of spine landmarks. The distinct feature of this composite network is that it can consider the mechanistic contribution in spine growth along with pure data.

Calibrating neural network (FFNN_{ca}): The governing physical equation of bone growth described in Section 3 is implemented in the calibrating part.

The framework of the calibrating part is shown in Fig. 12. The inputs are the stress values at each landmark $\boldsymbol{\sigma} = [\sigma_{11}, \sigma_{12}, \sigma_{13}, \sigma_{22}, \sigma_{23}, \sigma_{33}]$. The nodes corresponding to each landmark are identified in the finite element model explained in Section 2 using surface registration. For each landmark, the surrounding nodes which have the shared surface with the corresponding node are identified as well. These nodes along with the landmark points are used to calculate the average stress which is the input of the neural network as shown in Fig. 13. The outputs are the growth rates $\boldsymbol{G} = [G_1, G_2, G_3]$. In order to learn the trend of growth strain from stress, 1000 stress vectors $\boldsymbol{\sigma}^s (s = 1, 2...1000)$ are generated by the uniform distribution within the range of possible stress values obtained from the finite element model. The range of each stress component is shown in Fig. 12. The corresponding growth strains of 1000 training samples $\boldsymbol{G}$ are generated by Eq. (3). The patient specific parameters $\boldsymbol{G^m}$ and $\boldsymbol{\beta}$ are pre-defined with an initial value using [38]. The calibrating neural network has ten neurons and one hidden layer. For training the neural network, the equations used during optimization are:

$$
\begin{aligned}
&find \;\; W_{ij}^l, \; b_j^l \; to \; minimize \\
&\qquad MSE = \frac{1}{N_T} \sum_{s=1}^{N_T} \left(\boldsymbol{G}^s - \bar{\boldsymbol{G}}^s(\boldsymbol{\sigma}) \right)^2, \\
&where \; \boldsymbol{G}^s = \mathscr{F}_{\text{FFNN}_{\text{ca}}}(\boldsymbol{\sigma}, W_{ij}^l, b_j^l), \\
&\qquad \bar{\boldsymbol{G}}^s(\sigma) \; is \; from \; physics \; dataset \; generated \; by \; \text{Eq. (3)}.
\end{aligned}
\tag{8}
$$

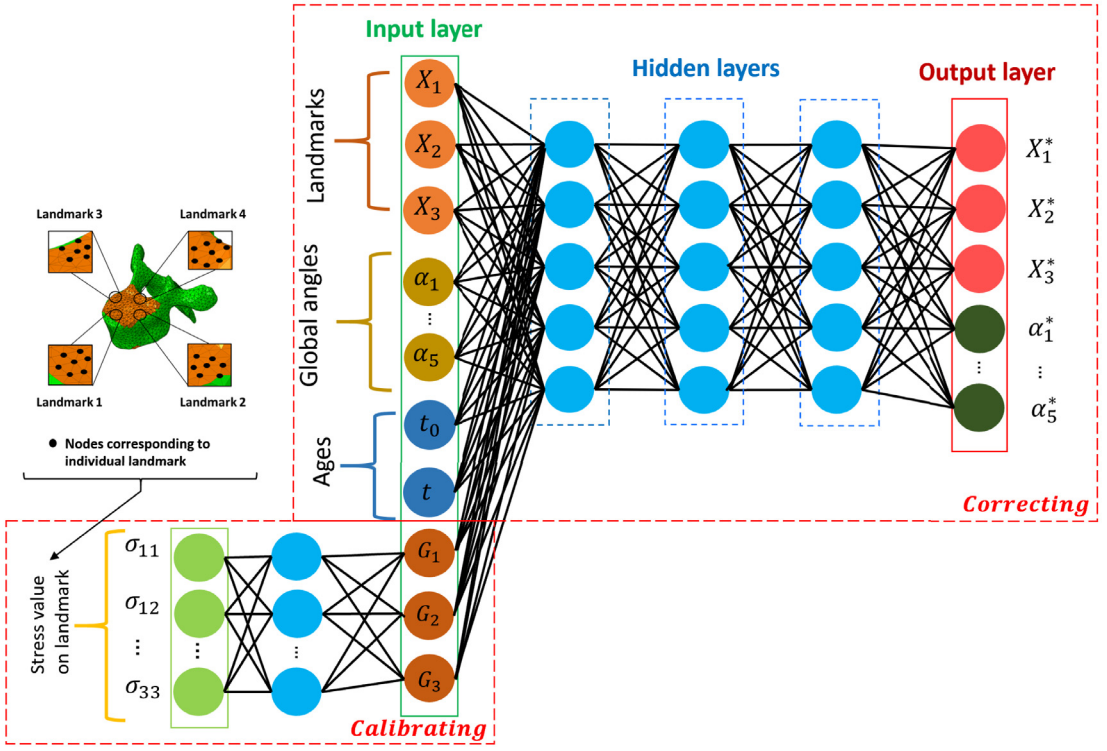

Fig. 13. Mechanistic Neural Network ($FFNN_m$) combining physics data and clinical data. The calibrating $FFNN_{ca}$ is trained by empirical equations and the correcting $FFNN_{co}$ is the neural network similar to pure data science approach.

After training the calibrating part, we get the "pre-trained" values of growth strain from the applied stress. Eq. (3) maps the stress on the growth plate to the growth rate. However, this is a linear equation which requires patient specific constants. With the aid of the calibrating NN, we may be able to capture the non-linear relationship between the growth rate and the stress. In addition, patient-specific constants will be calibrated in the convergence loop of the NN. Eq. (3) is just implemented to learn and carry out the first estimation of the growth rates.

Correcting neural network ($FFNN_{co}$): As shown in Fig. 13, the correcting neural network has a similar structure as the clinical neural network. The inputs of correcting part are the strain rate $\boldsymbol{G}$ and $\boldsymbol{I} = [\boldsymbol{X}, \boldsymbol{\alpha}, t_0, t]$. The outputs are $\boldsymbol{O} = [X_1^*, X_2^*, X_3^*, \alpha_1^*, \alpha_2^*, \alpha_3^*, \alpha_4^*, \alpha_5^*]$. The correcting neural network has 3 hidden layers and 10 neurons in each hidden layer.

Mechanistic neural network ($FFNN_m$): For this neural network, the input features are $\boldsymbol{\sigma}$ and $\boldsymbol{I}^s = [\boldsymbol{X}, \boldsymbol{\alpha}, t_0, t]$, similar to the input features for the pure data science training, as shown in Fig. 13. The outputs are the predicted positions for the landmarks defined as $\boldsymbol{X}^*, \boldsymbol{\alpha}^*$. This neural network consists of $FFNN_{ca}$ and $FFNN_{co}$.

$FFNN_{ca}$ is the physics neural network and trained by the physics dataset. After training, $FFNN_{ca}$ is combined with $FFNN_{co}$ to become the mechanistic neural network $FFNN_m$. The training equations of the whole mechanistic neural network are:

$$
\begin{aligned}
&find \;\; W_{ij}^l,\; b_j^l \;\; to \; minimize \\
&\qquad MSE = \frac{1}{N_T}\sum_{s=1}^{N_T}\left(\boldsymbol{O}^s - \bar{\boldsymbol{O}}^s\right)^2, \\
&where \;\; \boldsymbol{O}^s = [X_1^*, X_2^*, X_3^*, \alpha_1^*, \alpha_2^*, \alpha_3^*, \alpha_4^*, \alpha_5^*] = \mathscr{F}_{\mathrm{FFNN_m}}(\boldsymbol{I}^s, \boldsymbol{\sigma}, W_{ij}^l, b_j^l), \\
&\qquad \bar{\boldsymbol{O}}^s \; is \; from \; clinical \; dataset.
\end{aligned}
\tag{9}
$$

The aforementioned neural network structure can be explained as a specific application of Hierarchical Deep Learning Neural Network (HiDeNN) discussed in the companion paper by Saha et al. [16] and in [56]. HiDeNN

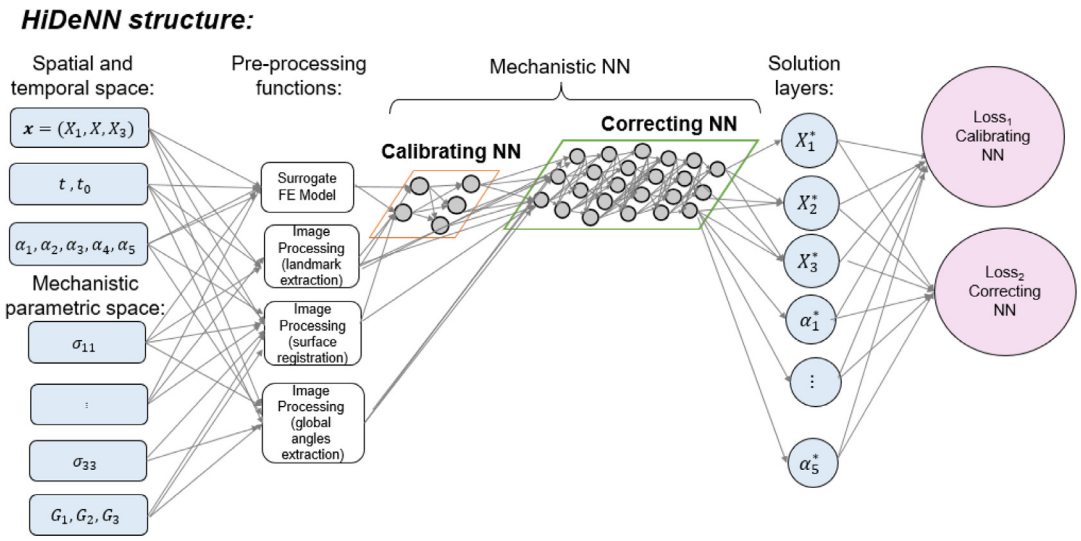

Fig. 14. Detailed construction of the proposed HiDeNN framework. The input layer takes in space, time, and mechanistic parameter variables of a system. The input layer is connected to the pre-processing function, Hierarchical DNNs, and finally the solution layer. Governing equations can be obtained from solution layers through the loss function.

was proposed to solve general class of challenging computational science and engineering problems. In [16], the challenging problems are classified based on available mechanistic knowledge and experimental data. The spine problem is in the category of problems where insufficient mechanistic knowledge with small amount of experimental data are available. In such cases, the prescription is to device the HiDeNN structure in such a way that we can combine the mechanistic knowledge and experimental data. For predicting spine growth, as shown in Fig. 14, the spine curvature, age, and five global angles are considered as variables in spatial and temporal spaces. Mechanistic information consists of 6 stress components and 3 growth strain rate on each landmark which are in the mechanistic parametric space. The pre-processing functions are used to develop the surrogate FE model and extract images. After pre-processing, the calibrating neural network is used to learn the mechanistic insight whereas the correcting neural network is learning from the clinical data. The calibrating and correcting neural networks form the mechanistic neural network part of HiDeNN. The solution layer will give the positions and angles of the deformed spine. The loss function is coming from both calibrating NN (mechanistic constraint) and correcting NN (difference between the ground truth and trained data).

The whole framework of the mechanistic neural network of the HiDeNN is shown in Fig. 15. After generating the 3D geometry of the spine, stress values are calculated using the finite element models. The growth rates are calculated by the calibrating part and then passed to the mechanistic neural network. After predicting the spine shape and global angles, the spine geometry is constructed. During training, this newly constructed geometry was used to compute the stress at different ages. However, for online stage these values can be directly taken as the future state of the spine.

The Levenberg–Marquardt method [57] is used as the optimization method for training all the neural networks. After the training stage, the combination of the two neural networks has the capability to consider the influence of stress on the bone growth.

4.3. Results

4.3.1. Patient 1 (single curvature)

Fig. 16(a) shows the predictions at the age of 68 months (inside of the range of the trained data). In order to better describe the results, we only show three central points of each vertebra here (the centre point of top, middle and bottom plane). It is obvious that the mechanistic neural network achieves a more accurate prediction compared with the clinical neural network. Fig. 16(b) shows the prediction at an age outside of the range in dataset (39–123

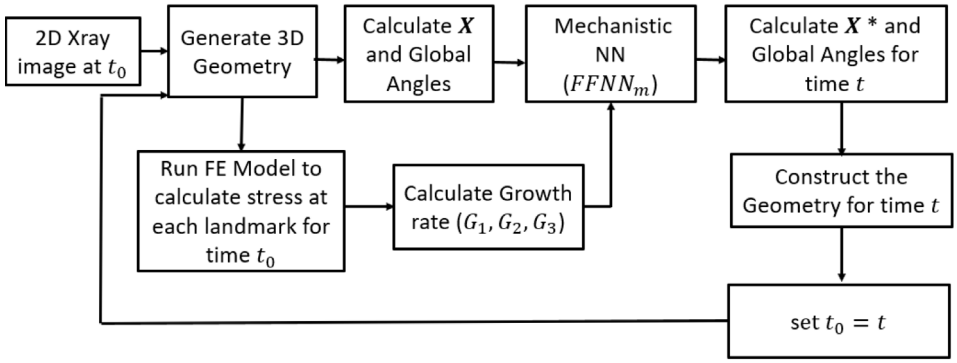

Fig. 15. Workflow for the mechanistic neural network ($FFNN_m$).

Table 9
Relative approximation error of the clinical neural network and the mechanistic neural network for Patient 1.

Type of NN	Ages included in stress datasets	Prediction inside		Prediction outside
		68 months	84 months	127 months
Clinical NN	–	10.08%	19.67%	7.66%
Mechanistic NN-1	39	1.37%	2.55%	0.89%
Mechanistic NN-2	39, 66	1.14%	2.55%	0.66%
Mechanistic NN-3	39, 66, 86	0.60%	1.28%	0.28%

months). Thus, the mechanistic neural network has the capability of predicting outside of range of the dataset. It is not surprising that for this patient the Clinical NN is acceptable for both inside and outside of the range of the prediction despite having a few data points. At 68 months, the Clinical NN is doing the interpolation between the trained input data, and the prediction obtained at 127 months is only 4 months after the last input dataset. As observed later for Patient 2, the prediction obtained from the Clinical NN and Mechanistic NN varies significantly as we go further from the input datasets. The $3D$ reconstruction of the prediction results inside the range of the training data and the reconstructed $3D$ geometry of the training data (66 and 100 months) are shown in Fig. 17 using the Mechanistic NN which indicates a good agreement with the experimental data.

The relative approximation error is calculated as

$$\delta = \frac{\frac{1}{S}\sum_{s=1}^{S} \|\boldsymbol{X}^s - \bar{\boldsymbol{X}}^s\|}{l} \times 100\%, \tag{10}$$

where δ is the relative error, $s = 1, 2...S$ is the index of central landmarks in a spine. $\boldsymbol{X}^s$ are the predicted landmarks, $\bar{\boldsymbol{X}}^s$ are the ground truth landmark positions, and $\|.\|$ is the L^2 norm. The width of spine at the current age is l. The error of each test case is shown in Table 9. Depending on the number of finite element models used for the calibration, the Mechanistic NN-1 used stress values obtained at the age of 39 months and the Mechanistic NN-2 used stress values obtained at the age of 39 and 66 months. The Mechanistic NN-3 used stress values obtained at the age of 39, 66 and 86 months. It is obvious that our mechanistic neural network yields a much more accurate prediction than the Clinical neural network with more physics involved.

As described, the mechanistic framework can also predict the age not included in the training database. This is because the stress and growth strain rate can reveal information about the trend of the predicted data. In addition, the stress distribution affects the growth rate and the forces applied during the treatment procedure influence the growth distribution. A mechanistic neural network can also use the physical equations to predict possible effects made by the forces applied during the treatment procedure.

It should be noted that adding more data into the Clinical NN can improve the interpolation results while providing helpful prognostic information for outside of the range if the extrapolation is not far from the training data as presented in Fig. 16. However, as will be presented later for Patient 2 (Fig. 18), the forecasted results degrade as one gets further from the input dataset.

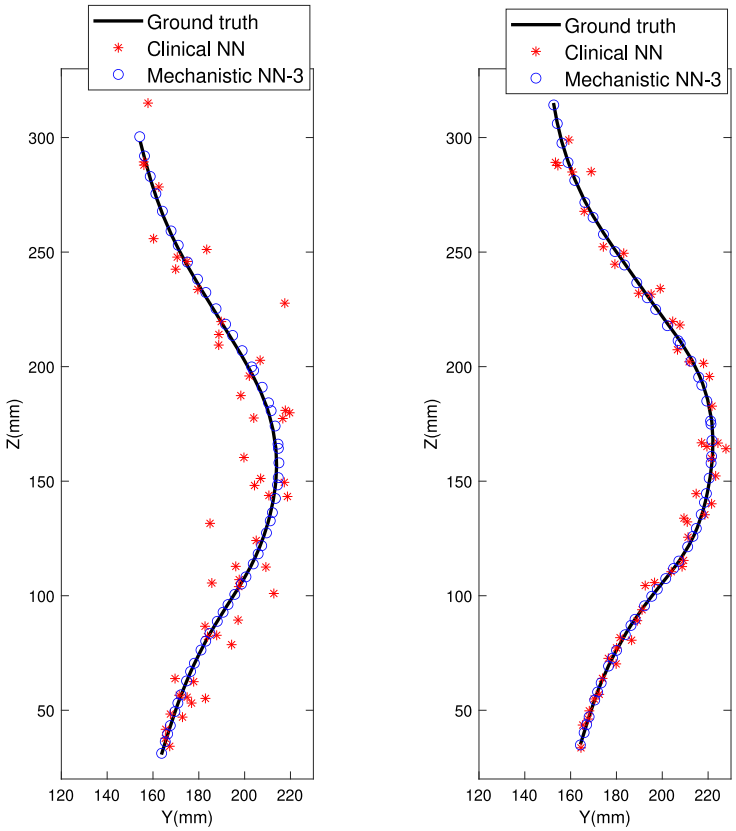

Fig. 16. Differences between pure data science prediction (clinical NN) and hybrid neural network prediction (Mechanistic NN-3) for Patient 1 (single curvature) at age of (a) 68 Months (inside of the range of the trained data), and (b) 127 Months (outside of the range of the trained data). The landmarks are three central points of each vertebra (the centre point of bottom, mid and top planes of each vertebra). It is obvious that the Mechanistic NN is closer to the ground truth.

The nature of the mechanistic machine learning relies on combining the kinematics and kinetics information of the landmarks from the surrogate model and obtaining the trend of the predicted output data from clinical information (X-ray images). Thus, the only component that provides the information outside of the range is the surrogate model.

The proposed mechanistic machine learning algorithm can significantly improve the accuracy of spine curvature prediction as compared to the clinical neural network. It can also predict the spine curvature at ages not included in the training database. However, the current model has some limitations. The current framework is based on the input of the stress values from finite element model at the age of 39, 66 and 86 months. As described in Table 9, incorporating more stress data sets can increase the prediction accuracy. We can include more inputs from finite element models at more time frames to further increase the prediction accuracy. In addition, the applied loads and boundary conditions are simplified and do not account for the effect of the surrounding tissue and daily activity.

4.3.2. Patient 2 (double curvature) results and cross validation on the data

To demonstrate the accuracy of the mechanistic neural network prediction, here we present the results obtained from the second patient. The procedure of reconstructing the NN is the same as described for the first patient. The training and testing data are described in Table 10. The comparison between the results of the ground truth (real data taken from X-ray images), Clinical NN and Mechanistic NN are shown in Fig. 18 using five stress datasets on age (month): 124, 139, 149, 160, 168. From Fig. 18, the Clinical NN can predict the spine curvature within the

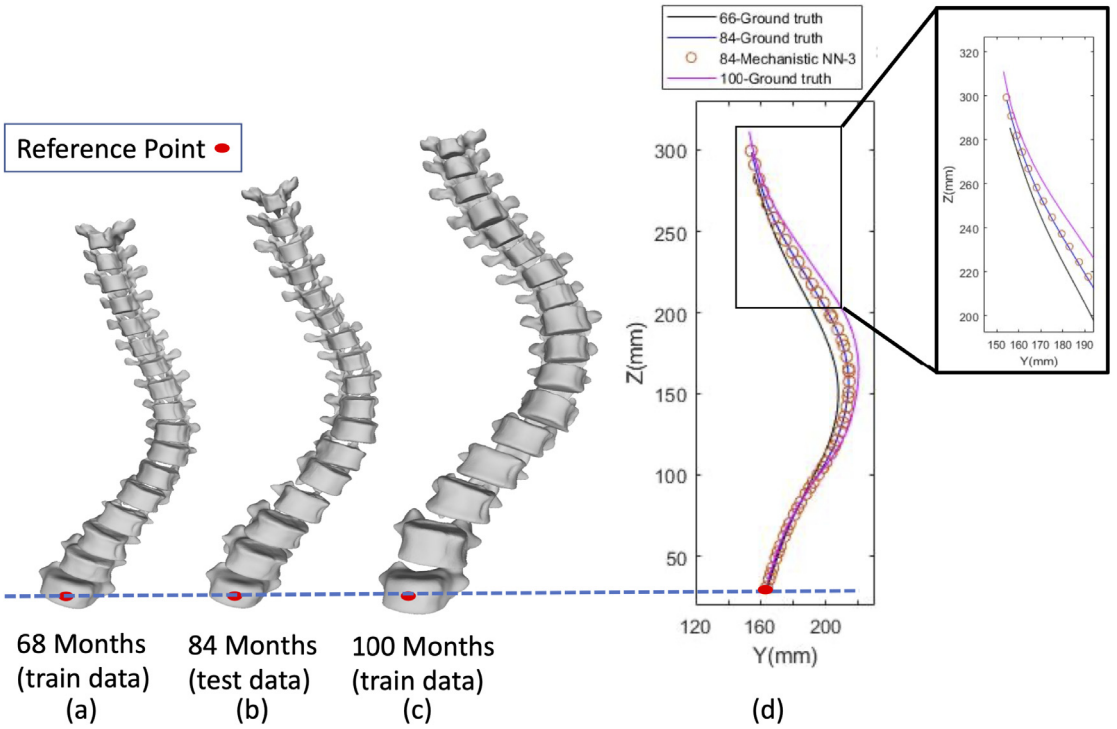

Fig. 17. The reconstructed 3D geometry of Patient 1 (single curvature) using *Mechanistic NN-3* for inside of the range prediction, (a) the 68 Months is the train data, (b) 84 Months is the test data, (c) the 100 Months is the train data, and (d) comparison between the predicted results and the ground truth (real data). The landmarks are three central points of each vertebra (the centre point of bottom, mid and top planes of each vertebra). For comparison of the height and spinal column growth over time, the reference point of all three configurations are shown by the red dot.

Table 10
Data collection for the clinical and mechanistic neural network for Patient 2.

Identification of X-ray images	Age (months)
Initial X-ray image	124
Training X-ray images	{139, 149, 160, 168}
X-ray images for comparing with results from NN	{156, 179, 187}

training dataset range however has deviations in predicting outside the range. Mechanistic NN has a better prediction compared with Clinical NN and is closer to the real spine curvature. Depending on the number of stress datasets extracted from the surrogate model, the prediction error varies as described in Table 11. It shows that with more sets of stress data, the accuracy of prediction increases. The $3D$ reconstruction of the prediction results inside and outside of the range of the training data and the reconstructed $3D$ geometry of the predicted data (156, 179 and 187 months) are shown in Fig. 19 using the Mechanistic NN which indicates a good agreement with the experimental data. To find out how the input and output data affect the framework error, a cross validation study is done as shown in Table 12. Cross validation explains how accurately a predictive model will perform in practice [58]. Since we focus more on prediction outside of the range, we keep the last two ages as the test cases and rotate the test case within previous age period. From Table 12, we can observe that the prediction error of Mechanistic NN is always below the Clinical NN and can predict the future spinal curvature with a relatively small error.

5. Conclusion and future work

The proposed work combines biomechanics, finite element analysis, advanced data science and image analysis technique to develop a predictive, patient-specific model for spine curvature in AIS patients. Our research addresses

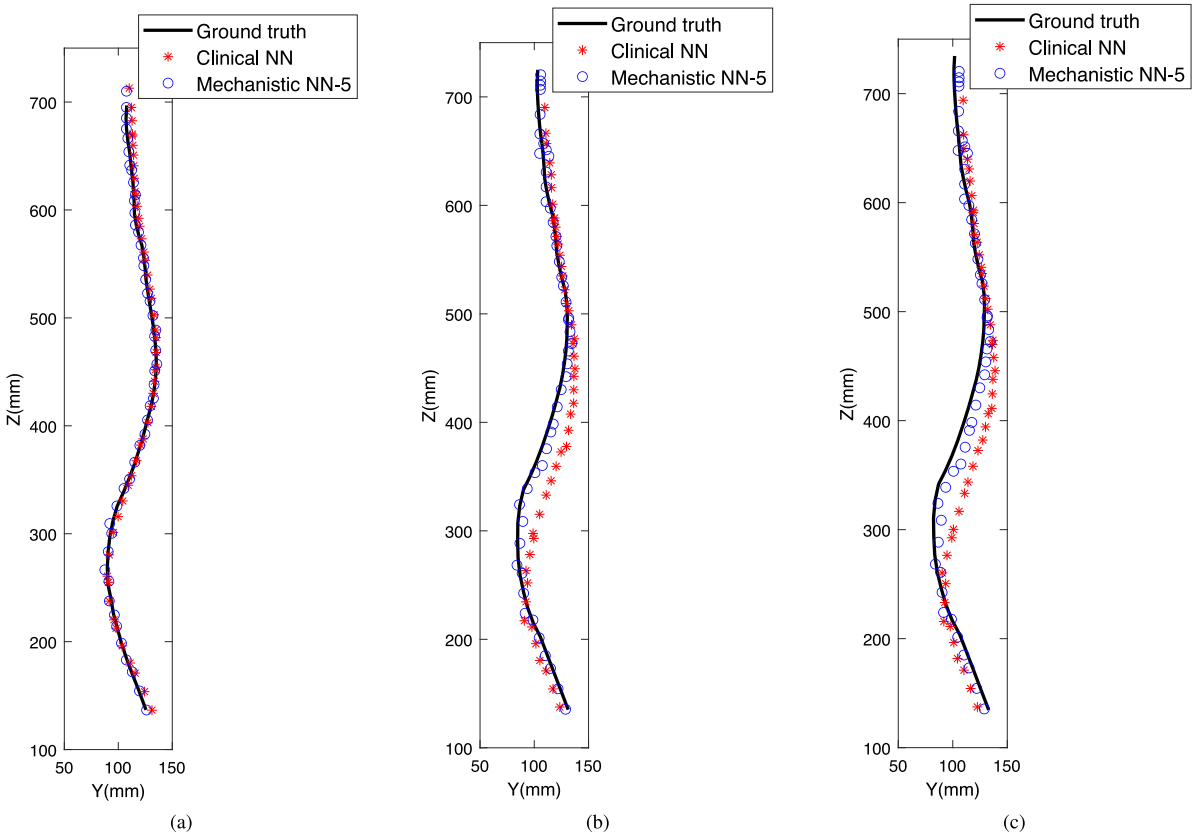

Fig. 18. Differences between pure data science prediction (Clinical NN) and hybrid neural network prediction (Mechanistic NN-5) and ground truth (the results obtained by X-ray images) for Patient 2 (double curvature) at age of (a) 156 Months (inside of the range of the trained data), (b) 179 Months (outside of the range of the trained data), and (c) 187 Months (outside of the range of the trained data). The landmarks are three central points of each vertebra (the centre point of bottom, mid and top planes of each vertebra). It is obvious that the Mechanistic NN-5 is closer to the ground truth.

Table 11
Relative approximation error of the clinical neural network and the mechanistic neural network for Patient 2.

Type of NN	Ages included in stress datasets	Prediction inside	Prediction outside	
		156	179	187
Clinical NN	–	4.38%	20.14%	31.70%
Mechanistic NN-1	124	5.14%	24.16%	35.90%
Mechanistic NN-2	124, 139	3.12%	16.72%	22.45%
Mechanistic NN-3	124, 139, 149	1.17%	9.82%	16.59%
Mechanistic NN-4	124, 139, 149, 160	1.06%	6.51%	12.44%
Mechanistic NN-5	124, 139, 149, 160, 168	0.70%	4.38%	10.43%

the issues of limited data for validation of AIS model, variability of spinal growth among different patients and complexity of geometrical features of spines for predicting curvature. To develop the system, Lurie Hospital provided the X-ray images of spine from AIS patients at different ages, treatment stages, and physical conditions. By incorporating a mechanistic learning and physical simulation model along with clinical data, we design a mechanistic neural network that can predict the spinal curve progression with time for a specific patient. The novelty of the proposed method lies in its generality in predictive capability i.e. unlike the traditional neural networks, it can predict outside the range of conditions specified in the training data. As mentioned in Section 3, a surrogate spine model is used to obtain the trend of the predicted data used in the *Mechanistic NN*. In the future work, calibration

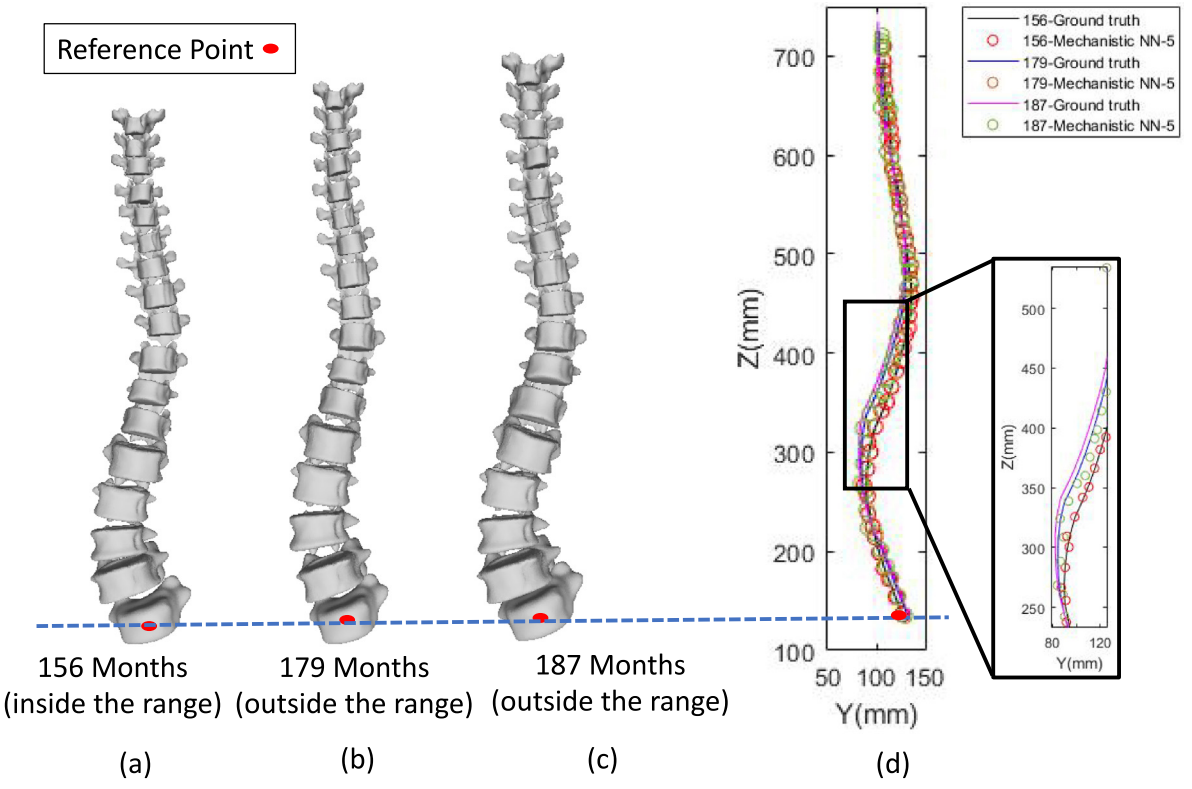

Fig. 19. The reconstructed 3D geometry of Patient 2 (double curvature) using *Mechanistic NN-5* for prediction inside and outside of the range of the training data, (a) the 156 Months is inside of the range, (b) 179 Months is outside of the range, (c) the 187 Months is outside of the range, and (d) comparison between the predicted results (*Mechanistic NN-5*) and the ground truth (real data). The landmarks are three central points of each vertebra (the centre point of bottom, mid and top planes of each vertebra). For comparison of the height and spinal column growth over time, the reference point of all three configurations are shown by the red dot.

Table 12
Cross validation study on Patient 2. For each case, the testing data (blue cells) and training data (white cells) are shown. The relative approximation error is calculated for each prediction case.

Months	Ages included in stress datasets	Validation performance using the training datasets						Prediction performance	
		124	139	149	156	160	168	179[a]	187[a]
Clinical NN	–	5.66%						17.65%	27.70%
Mechanistic NN-5	139, 149, 156, 160, 168	**2.18%**						**4.12%**	**10.64%**
Clinical NN	–		8.91%					16.02%	22.45%
Mechanistic NN-5	124, 149, 156, 160, 168		**1.05%**					**3.15%**	**11.66%**
Clinical NN	–			7.44%				15.45%	35.11%
Mechanistic NN-5	124, 139, 156, 160, 168			**3.25%**				**6.16%**	**10.79%**
Clinical NN	–				4.38%			20.14%	31.70%
Mechanistic NN-5	124, 139, 149, 160, 168				**0.70%**			**4.38%**	**10.43%**
Clinical NN	–					5.16%		17.24%	34.74%
Mechanistic NN-5	124, 139, 149, 156, 168					**1.54%**		**7.92%**	**13.29%**
Clinical NN	–						10.59%	22.84%	34.25%
Mechanistic NN-5	124, 139, 149, 156, 160						**5.63%**	**12.42%**	**18.42%**

[a]Prediction at age outside of the range of trained data.

Table 13
Number of elements (N_E) and nodes (N_V) based on the optimally designed size of face triangle meshes in Appendix A, and the optimally designed mesh size (S) of the 3D finite element meshes of each vertebra and intervertebral disc (IVD).

Vertebra	N_E	N_V	S (mm)	IVD	N_E	N_V	S (mm)
L1	16,658	3,761	1.33	$L_{1,2}$	15,572	3,393	1.24
L2	16,168	3,685	1.19	$L_{2,3}$	14,988	3,251	1.36
L3	16,852	3,612	1.09	$L_{3,4}$	15,678	3,444	1.16
L4	16,165	3,687	1.24	$L_{4,5}$	17,106	3,788	1.42
L5	16,999	3,830	1.18	$T_{1,2}$	14,995	3,356	1.40
T1	22,845	4,762	1.07	$T_{2,3}$	15,225	3,296	0.909
T2	24,132	4,960	1.11	$T_{3,4}$	14,842	3,263	1.09
T3	22,631	4,762	1.18	$T_{4,5}$	16,246	3,551	1.14
T4	24,388	5,012	0.958	$T_{5,6}$	14,167	3,078	0.983
T5	24,221	5,005	0.956	$T_{6,7}$	16,249	3,514	1.09
T6	25,404	5,187	0.984	$T_{7,8}$	15,104	3,260	0.844
T7	25,808	5,255	0.953	$T_{8,9}$	14,680	3,217	0.960
T8	24,151	4,979	1.17	$7T_{9,10}$	14,962	3,266	0.783
T9	22,475	4,729	0.954	$T_{10,11}$	13,721	2,957	0.949
T10	17,830	3,949	1.02	$T_{11,12}$	13,453	2,916	1.03
T11	17,549	3,919	1.15	T_1L_5	18,257	3,726	0.950
T12	17,024	3,834	1.14				

Table 14
Mechanical properties of cortical bone with time (data given as mean) for infant [59–61].

Age (months)	Elastic modulus (MPa)
$\leqslant 1$	451.7
(1, 2]	645.8
(2, 3]	768.8
(3, 4]	768.8
(4, 5]	796.4
(5, 6]	886.1
(6, 7]	992.6
(7, 8]	1,980.3
(8, 9]	1,467.12
(9, 10]	1,417.9
(10, 11]	1,232.5
(11, 24]	1,848
(24, 36]	1,909
(36, 48]	1,883
(48, 60]	2,068
(60, 72]	2,155
(72, 120]	1,988
(120, 158]	1,995

of material properties and boundary conditions can be performed to study their effect on the prediction error along with improving the robustness of the surrogate model using the ample number of *in vitro* and *in vivo* results from experiments. To investigate the effect of each contributing factor on the prediction error of the mechanistic framework, further sensitivity analysis is required regarding the noise in the input data of the *Mechanistic NN* and the mesh size of the surrogate model. The generality stems from the improved physical and material models used in the computational method. In the computational model, varying material properties in different parts of the spine are considered. In addition, the model contains patient-specific constants that can handle the patient-specific variability in material properties. Patient-specific models of the spines are generated through image segmentation and surface registration methods with the help of clinical X-ray image data from Lurie Hospital. These techniques can handle the complex geometry of vertebrae in human spine for 3D reconstructions. Thus, the proposed method has improved capability to capture progressive change in spine curvature for a specific patient compared to the existing models.

The physicians require real-time prediction of curvature in spine of AIS patients to prescribe most suitable path of treatment. If braces are to be designed for treatments, the design must consider the change in the shape of AIS patient's spine over the period of treatment. Therefore, the brace designers also require a real-time predictive scheme for proper design. Our proposed methodology offers a predictive scheme while considering all the complex factors including geometry, material property, physical conditions, etc. For fast calculation we will develop a physics-based reduced order model and incorporate it into our computational framework. Moreover, the geometric update will also be performed based on unsupervised learning assisted clusters on vertebral growth plates. Thus, the model will be able to calculate and predict the shape of vertebrae very quickly and the physicians can visualize the progression of spine in real time. This will be another unique feature of the proposed model making it suitable for direct implementation in hospitals. The entire methodology is very general from computational point of view and can be adopted to treat other spinal diseases like Lordosis and Kyphosis. Therefore, the scheme has broader impact on the treatment of spinal deformities.

Declaration of competing interest

The authors declare that they have no known competing financial interests or personal relationships that could have appeared to influence the work reported in this paper.

Acknowledgements

We would like to thank the Division of Orthopaedic Surgery and Sports Medicine at Ann and Robert H. Lurie Children's Hospital for their collaboration on this project made possible by a philanthropic grant. W.K. Liu, S. Saha, and H. Li would like to acknowledge the support of National Science Foundation (NSF) CMMI-1762035. M. Tajdari would like to thank Sarah Ziselman for her assistance in data processing. A. Pawar and Y.J. Zhang were supported in part by the NSF grants CMMI-1953323, CBET-1804929 and a PITA (Pennsylvania Infrastructure Technology Alliance) grant. Moreover, F. Tajdari is partly supported by Dutch NWO Next UPPS — Integrated design methodology for Ultra Personalized Products and Services project.

Appendix A. Optimal uniform mesh size

Assume M is an intermediate mesh model and suppose the simulation mesh models as A_i $(i = 1, 2, \ldots, n)$ and the hybrid mesh size [62] field as D_{mix}. In addition, suppose the optimized mesh of the primary mesh M in the first step as M' with the node number m and assume its corresponding mesh size field as D'. The optimal problem [63,64] of the uniform intermediate mesh model can be formulated as:

$$\min J = J_1(X) + J_2(X) + J_3(X), \tag{11}$$

where

$$\begin{aligned} J_1(X) &= |D' - D_{mix}| = \sum_{j=1}^{m} |p_i - q_j|, \\ J_2(X) &= S = m, \\ J_3(X) &= \sum_{i=1}^{n} |A_i - D'| = \sum_{i=1}^{n} \left(\sum_{j=1}^{k_i} \min |o_j - p_j| \right), \end{aligned} \tag{12}$$

and $X = [\omega_1, \omega_1, \ldots, \omega_K]$, subject to,

$$1 \le \omega_i \le 1.5 \ (1 \le i \le K).$$

Accordingly, ω_i is a weight for node size interval in order to define the specific degree of refinement at the corresponding hybrid node size. X corresponds to the intermediate mesh model. J presents the optimization objective and S is the minimum node number of M'. p_j, q_j, and o_j are essentially the node sizes of the j_{th} node in the D', D_{mix} and the mesh size field of a simulation mesh model, respectively. In addition, the first optimization objective $J_1(.)$ is employed to minimize the node size deviation for the mesh nodes and discrete nodes of the intermediate mesh model and accordingly their correspondences in the hybrid mesh size field. The second

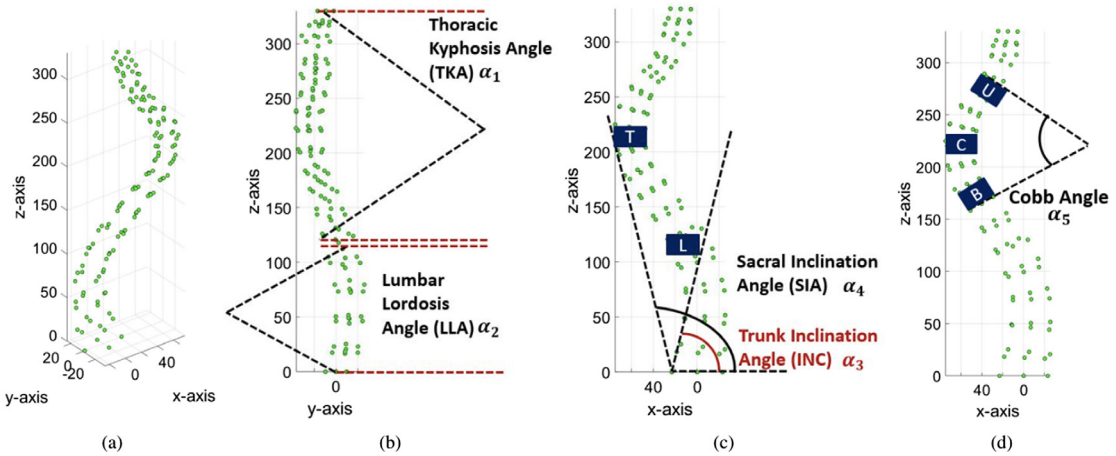

Fig. 20. Description of the five global angles (α_i). (a) 3D configuration of the spine. The green points describe the landmarks of the spine; (b) Thoracic Kyphosis Angle (TKA) and Lumbar Lordosis Angle (LLA) in z–y plane; (c) Sacral Inclination Angle (SIA) and Trunk Inclination Angle (INC) in the z–x plane; and (d) Cobb Angle in the z–x plane.

minimization objective $J_2(.)$ is recruited to minimize the number of intermediate mesh nodes. Ultimately, the last minimization objective $J_3(.)$ is utilized to minimize the nearest distance between the intermediate mesh nodes and heterogeneous simulation mesh nodes.

Appendix B. Five global angles of spine

The five global angles are used to describe the shape of the spine [65]:

- α_1, Thoracic Kyphosis Angle (TKA);
- α_2, Lumbar Lordosis Angle (LLA);
- α_3, Trunk Inclination Angle (INC);
- α_4, Sacral Inclination Angle (SIA); and
- α_5, Cobb Angle.

The Thoracic Kyphosis Angle (TKA) α_1 is defined as the angle between the top plane of the T1 vertebrae and the bottom plane of the T12 vertebrae [65] in the sagittal plane (plane z–y), see Fig. 20. The TKA quantifies the curvature of the Thoracic Spine. The Lumbar Lordosis Angle (LLA) α_2 is defined as the angle between the top plane of the L1 vertebrae and the bottom plane of the L5 vertebrae [65] in the sagittal plane, see Fig. 20. The LLA quantifies the curvature of the Lumbar Spine. In order to define the Trunk Inclination Angle α_3, the vertebrae where there is maximum curvature in the Lumbar Spine, L, is found. To define the Sacral Inclination Angle (INC) α_4, the vertebrae where there is maximum curvature in the Thoracic spine, T, is found Fig. 20. The Cobb Angle is utilized by the Scoliosis Research Society to measure spinal deformities. However, there is no universal way to measure the Cobb Angle of a spine. In order to define the Cobb Angle within this study, the vertebrae where there is maximum curvature in the Thoracic spine is found, C, see Fig. 20. U and B will be the vertebrae that are three above and three below vertebrae C, respectively. The Cobb Angle is defined as the angle between the top plane of U and the bottom plane of B on the frontal plane (plane $z-x$).

Appendix C. Validation of the surrogate finite element model of spine

The results of the generated finite element model are used to calculate the stress located on the top and bottom surfaces of each vertebra, which can provide a trend for prediction. The calculated stress will be used as an input for the mechanistic neural network for the prediction of curve progression. There are some methods to validate the results obtained by the spine finite element model. In this paper, the intervertebral disc (IVD) pressure is validated with the *in vitro* results provided in [66]. One critical parameter to characterize spinal load and effect on the spine curve progression is IVD pressure. This parameter is among the few criteria that are directly controlled

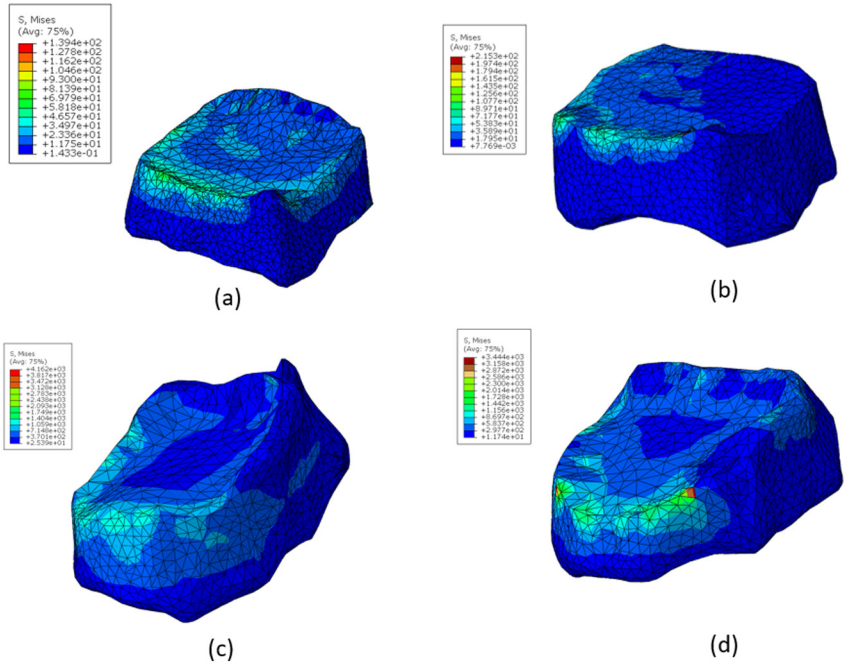

Fig. 21. Von Mises stress distribution on intervertebral disc between (a) L3 and L4 vertebrae, (b) L3 and L4 vertebrae, (c) T1 and T2 vertebrae, and (d) T2 and T3 vertebrae (10^2 Pa).

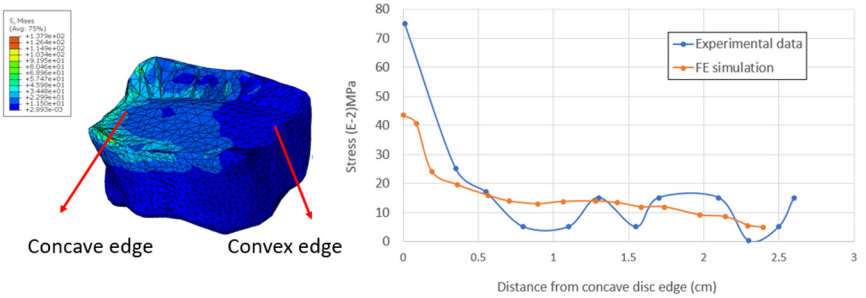

Fig. 22. Comparison of von Mises stress distribution of simulation and experimental data on disc L_{12} [68].

by the axial spinal load [67]. Maximum physiological IVD pressure is assumed to be between 0.1 MPa and 0.24 MPa [66]. However, scoliotic spine has higher pressure compared to the control patients. Fig. 21 demonstrates the von Mises stress distribution on IVD generated using ABAQUS software. As can be seen, the stress distribution is not symmetric on IVD (as it is expected) which leads to non-uniform growth of the vertebra and progression of scoliosis.

The distribution of the von Mises stress can be compared with the experimental data provided in [68] in the intervertebral disc between L1 and L2 vertebrae (Fig. 22). The stress is plotted along the path between concave and convex edges in the absence of muscle load. Since the experimental data is not taken from the same patient as the geometry in the finite element simulation, the maximum stress value is not the same. However, the distribution and range of the stresses are similar. The only purpose to visualize the comparison with the experimental data is demonstrating the not-symmetry trend of the stress distribution, and the magnitude of the stress should not be compared since the results are taken from different geometry with different material properties. As mentioned earlier in Section 3, the generated model is a surrogate model and we used the *indirect* validation method described in [37]. Indirect validation uses the experimental data that is not controlled by the user. This type of validation may seem unfavourable but it is unavoidable in this study since the *in vivo* IVD stress distribution results of the distinct

geometry is not available. Moreover, in this study the sensitivity analysis on the mesh size is not required in the surrogate model since the results extracted from the surrogate model provide the trend of the output data used in the Mechanistic NN.

References

[1] I.A.F. Stokes, Mechanical effects on skeletal growth, J. Musculoskelet. Neuronal Interact. 2 (3) (2002) 277–280.
[2] I. Villemure, C. Aubin, J. Dansereau, H. Labelle, Biomechanical simulations of the spine deformation process in adolescent idiopathic scoliosis from different pathogenesis hypotheses, Eur. Spine J. 13 (1) (2004) 83–90.
[3] I.A. Stokes, Analysis and simulation of progressive adolescent scoliosis by biomechanical growth modulation, Eur. Spine J. 16 (10) (2007) 1621–1628.
[4] X. Drevelle, Y. Lafon, E. Ebermeyer, I. Courtois, J. Dubousset, W. Skalli, Analysis of idiopathic scoliosis progression by using numerical simulation, Spine 35 (10) (2010) E407–E412.
[5] A. Van Der Plaats, A. Veldhuizen, G.J. Verkerke, Numerical simulation of asymmetrically altered growth as initiation mechanism of scoliosis, Ann. Biomed. Eng. 35 (7) (2007) 1206–1215.
[6] J. Fok, S. Adeeb, J. Carey, FEM simulation of non-progressive growth from asymmetric loading and vicious cycle theory: scoliosis study proof of concept, Open Biomed. Eng. J. 4 (2010) 162.
[7] A. Rajkomar, J. Dean, I. Kohane, Machine learning in medicine, New Engl. J. Med. 380 (14) (2019) 1347–1358.
[8] J.A. Sidey-Gibbons, C.J. Sidey-Gibbons, Machine learning in medicine: a practical introduction, BMC Med. Res. Methodol. 19 (1) (2019) 64.
[9] A. Esteva, A. Robicquet, B. Ramsundar, V. Kuleshov, M. DePristo, K. Chou, C. Cui, G. Corrado, S. Thrun, J. Dean, A guide to deep learning in healthcare, Nature Med. 25 (1) (2019) 24–29.
[10] Z. Obermeyer, E.J. Emanuel, Predicting the future — big data, machine learning, and clinical medicine, New Engl. J. Med. 375 (13) (2016) 1216.
[11] H.A. Haenssle, C. Fink, R. Schneiderbauer, F. Toberer, T. Buhl, A. Blum, A. Kalloo, A.B.H. Hassen, L. Thomas, A. Enk, et al., Man against machine: diagnostic performance of a deep learning convolutional neural network for dermoscopic melanoma recognition in comparison to 58 dermatologists, Ann. Oncol. 29 (8) (2018) 1836–1842.
[12] J. Yang, K. Zhang, H. Fan, Z. Huang, Y. Xiang, J. Yang, L. He, L. Zhang, Y. Yang, R. Li, et al., Development and validation of deep learning algorithms for scoliosis screening using back images, Commun. Biol. 2 (1) (2019) 1–8.
[13] W. Thong, S. Parent, J. Wu, C.-E. Aubin, H. Labelle, S. Kadoury, Three-dimensional morphology study of surgical adolescent idiopathic scoliosis patient from encoded geometric models, Eur. Spine J. 25 (10) (2016) 3104–3113.
[14] E. García-Cano, F.A. Cosío, L. Duong, C. Bellefleur, M. Roy-Beaudry, J. Joncas, S. Parent, H. Labelle, Prediction of spinal curve progression in adolescent idiopathic scoliosis using random forest regression, Comput. Biol. Med. 103 (2018) 34–43.
[15] S. Kadoury, W. Mandel, M. Roy-Beaudry, M.-L. Nault, S. Parent, 3-D morphology prediction of progressive spinal deformities from probabilistic modeling of discriminant manifolds, IEEE Trans. Med. Imaging 36 (5) (2017) 1194–1204.
[16] S. Saha, Z. Gan, L. Cheng, J. Gao, O.L. Kafka, X. Xie, H. Li, M. Tajdari, H.A. Kim, W.K. Liu, Hierarchical deep learning neural network (HiDeNN): An artificial intelligence (AI) framework for computational science and engineering, Comput. Methods Appl. Mech. Engrg. 373 (2021) 113452.
[17] Y.J. Zhang, Geometric Modeling and Mesh Generation from Scanned Images, Vol. 6, CRC Press, 2016.
[18] F. Hefti, Pediatric Orthopedics in Practice, Springer Science & Business Media, 2007.
[19] H. Bennani, B. McCane, J. Cornwall, Three dimensional (3D) lumbar vertebrae data set, Data Sci. J. 15 (2016).
[20] Thoracic-vertebrae 3D models, https://sketchfab.com/tags/thoracic-vertebrae.
[21] S. Valette, J.M. Chassery, R. Prost, Generic remeshing of 3D triangular meshes with metric-dependent discrete Voronoi diagrams, IEEE Trans. Vis. Comput. Graphics 14 (2) (2008) 369–381.
[22] I.M.G. Jakobsen, M. Plocharski, Automatic detection of cervical vertebral landmarks for fluoroscopic joint motion analysis, in: Scandinavian Conference on Image Analysis, Springer, 2019, pp. 209–220.
[23] H. Anitha, G. Prabhu, Automatic quantification of spinal curvature in scoliotic radiograph using image processing, J. Med. Syst. 36 (3) (2012) 1943–1951.
[24] P. Perona, J. Malik, Scale-space and edge detection using anisotropic diffusion, IEEE Trans. Pattern Anal. Mach. Intell. 12 (7) (1990) 629–639.
[25] M. Kass, A. Witkin, D. Terzopoulos, Snakes: active contour models, Int. J. Comput. Vis. 1 (4) (1988) 321–331.
[26] C. Xu, J.L. Prince, Gradient vector flow: a new external force for snakes, in: Proceedings of IEEE Computer Society Conference on Computer Vision and Pattern Recognition, 1997, pp. 66–71.
[27] Q. Rizqie, C. Pahl, D. Dewi, M. Ayob, I. Maolana, R. Hermawan, R. Soetkino, E. Suprivanto, 3D coordinate reconstruction from 2D X-ray images for guided lung biopsy, WSEAS Trans. Biol. Biomed. EISSN (2014) 2224–2902.
[28] H. Abdelmunim, A.A. Farag, Elastic shape registration using an incremental free form deformation approach with the ICP algorithm, in: Canadian Conference on Computer and Robot Vision, IEEE, 2011, pp. 212–218.
[29] X. Huang, N. Paragios, D. Metaxas, Establishing local correspondences towards compact representations of anatomical structures, in: International Conference on Medical Image Computing and Computer-Assisted Intervention, Springer, 2003, pp. 926–934.
[30] A. Pawar, Y.J. Zhang, C. Anitescu, Y. Jia, T. Rabczuk, DTHB3D_Reg: dynamic truncated hierarchical B-spline based 3D nonrigid image registration, Commun. Comput. Phys. 23 (3) (2018) 877–898.

[31] A. Pawar, Y. Zhang, Y. Jia, X. Wei, T. Rabczuk, C.L. Chan, C. Anitescu, Adaptive FEM-based nonrigid image registration using truncated hierarchical B-splines, Comput. Math. Appl. 72 (8) (2016) 2028–2040.
[32] Y. Shao, Y. Liu, X. Ye, H. Wang, A uniform intermediate model for high-fidelity and efficient visualisation of multidisciplinary heterogeneous simulation data, Int. J. Comput. Integr. Manuf. 29 (6) (2016) 591–610.
[33] Q. Fang, Mesh-based Monte Carlo method using fast ray-tracing in Plücker coordinates, Biomed. Opt. Express 1 (1) (2010) 165–175.
[34] M. Khosrow-Pour, Dictionary of Information Science and Technology, Vol. 1, IGI Global, 2006.
[35] P.S. Palar, R.P. Liem, L.R. Zuhal, K. Shimoyama, On the use of surrogate models in engineering design optimization and exploration: The key issues, in: Proceedings of the Genetic and Evolutionary Computation Conference Companion, 2019, pp. 1592–1602.
[36] M. Dreischarf, T. Zander, A. Shirazi-Adl, C. Puttlitz, C. Adam, C. Chen, V. Goel, A. Kiapour, Y. Kim, K. Labus, et al., Comparison of eight published static finite element models of the intact lumbar spine: predictive power of models improves when combined together, J. Biomech. 47 (8) (2014) 1757–1766.
[37] H.B. Henninger, S.P. Reese, A.E. Anderson, J.A. Weiss, Validation of computational models in biomechanics, Proc. Inst. Mech. Eng. H 224 (7) (2010) 801–812.
[38] L. Shi, D. Wang, M. Driscoll, I. Villemure, W.C. Chu, J.C. Cheng, C.-E. Aubin, Biomechanical analysis and modeling of different vertebral growth patterns in adolescent idiopathic scoliosis and healthy subjects, Scoliosis 6 (1) (2011) 11.
[39] H. Leng, M.J. Reyes, X.N. Dong, X. Wang, Effect of age on mechanical properties of the collagen phase in different orientations of human cortical bone, Bone 55 (2) (2013) 288–291.
[40] A. Schultz, G. Andersson, R. Ortengren, K. Haderspeck, A. Nachemson, Loads on the lumbar spine. Validation of a biomechanical analysis by measurements of intradiscal pressures and myoelectric signals, J. Bone Joint Surg. Am. Vol. 64 (5) (1982) 713–720.
[41] A. Nachemson, The load on lumbar disks in different positions of the body, Clin. Orthop. Relat. Res. (1976-2007) 45 (1966) 107–122.
[42] K. Tinning, J. Acworth, Make your best guess: an updated method for paediatric weight estimation in emergencies, Emerg. Med. Aust. 19 (6) (2007) 528–534.
[43] C. Goldberg, F. Dowling, E. Fogarty, Adolescent idiopathic scoliosis: is rising growth rate the triggering factor in progression? Eur. Spine J. 2 (1) (1993) 29–36.
[44] J.O. Sanders, R.H. Browne, T.E. Cooney, D.N. Finegold, S.J. McConnell, S.A. Margraf, Correlates of the peak height velocity in girls with idiopathic scoliosis, Spine 31 (20) (2006) 2289–2295.
[45] M. Nissinen, M. Heliövaara, J. Seitsamo, M. Poussa, Trunk asymmetry, posture, growth, and risk of scoliosis. A three-year follow-up of Finnish prepubertal school children, Spine 18 (1) (1993) 8–13.
[46] L.B. Skogland, J.A. Miller, The length and proportions of the thoracolumbar spine in children with idiopathic scoliosis, Acta Orthop. Scand. 52 (2) (1981) 177–185.
[47] M. Ylikoski, Spinal growth and progression of adolescent idiopathic scoliosis, Eur. Spine J. 1 (4) (1993) 236–239.
[48] G. Hägglund, J. Karlberg, S. Willner, Growth in girls with adolescent idiopathic scoliosis, Spine 17 (1) (1992) 108–111.
[49] J.A. Janicki, B. Alman, Scoliosis: Review of diagnosis and treatment, Paediatr. Child Health 12 (9) (2007) 771–776.
[50] C.A. Wise, X. Gao, S. Shoemaker, D. Gordon, J.A. Herring, Understanding genetic factors in idiopathic scoliosis, a complex disease of childhood, Curr. Genom. 9 (1) (2008) 51–59.
[51] I.A. Stokes, J.P. Laible, Three-dimensional osseo-ligamentous model of the thorax representing initiation of scoliosis by asymmetric growth, J. Biomech. 23 (6) (1990) 589–595.
[52] I.A. Stokes, H. Spence, D.D. Aronsson, N. Kilmer, Mechanical modulation of vertebral body growth: implications for scoliosis progression, Spine 21 (10) (1996) 1162–1167.
[53] C. Nash Jr, E. Gregg, R. Brown, K. Pillai, Risks of exposure to X-rays in patients undergoing long-term treatment for scoliosis, J. Bone Joint Surg. Am. Vol. 61 (3) (1979) 371–374.
[54] M. Wessels, Development of a Non-Fusion Scoliosis Correction Device: Designing and Testing (Ph.D. thesis), University of Twente, 2012.
[55] J. Han, C. Moraga, The influence of the sigmoid function parameters on the speed of backpropagation learning, in: International Workshop on Artificial Neural Networks, Springer, 1995, pp. 195–201.
[56] L. Zhang, L. Cheng, H. Li, J. Gao, C. Yu, R. Domel, Y. Yang, S. Tang, W.K. Liu, Hierarchical deep learning neural networks: Finite elements and beyond, Comput. Mech. (2020) Acceptance after minor revision.
[57] J.J. Moré, The Levenberg-Marquardt algorithm: implementation and theory, in: Numerical Analysis, Springer, 1978, pp. 105–116.
[58] M. Stone, Cross-validatory choice and assessment of statistical predictions, J. R. Stat. Soc. Ser. B Stat. Methodol. 36 (2) (1974) 111–133.
[59] Z. Fan, P.A. Smith, G.F. Harris, F. Rauch, R. Bajorunaite, Comparison of nanoindentation measurements between osteogenesis imperfecta type III and type IV and between different anatomic locations (femur/tibia versus iliac crest), Connect. Tissue Res. 48 (2) (2007) 70–75.
[60] C.G. Ambrose, M.S. Martinez, X. Bi, J. Deaver, C. Kuzawa, L. Schwartz, B. Dawson, A. Bachim, U. Polak, B. Lee, et al., Mechanical properties of infant bone, Bone 113 (2018) 151–160.
[61] Z. Altai, M. Viceconti, A.C. Offiah, X. Li, Investigating the mechanical response of paediatric bone under bending and torsion using finite element analysis, Biomech. Model. Mechanobiol. 17 (4) (2018) 1001–1009.
[62] E. Ruiz-Gironés, X. Roca, J. Sarrate, Combining size-preserving and smoothing procedures for adaptive quadrilateral mesh generation, in: Proceedings of the 22nd International Meshing Roundtable, Springer, 2014, pp. 19–37.
[63] F. Tajdari, C. Roncoli, M. Papageorgiou, Feedback-based ramp metering and lane-changing control with connected and automated vehicles, IEEE Trans. Intell. Transp. Syst. (2020).
[64] A. Khodayari, et al., A new model of car following behavior based on lane change effects using anticipation and evaluation idea, Iran. J. Mech. Eng. Trans. ISME 16 (2) (2015) 26–38.

[65] J. Miyazaki, S. Murata, J. Horie, A. Uematsu, T. Hortobágyi, S. Suzuki, Lumbar lordosis angle (LLA) and leg strength predict walking ability in elderly males, Arch. Gerontol. Geriatr. 56 (1) (2013) 141–147.
[66] T. Guehring, F. Unglaub, H. Lorenz, G. Omlor, H.-J. Wilke, M.W. Kroeber, Intradiscal pressure measurements in normal discs, compressed discs and compressed discs treated with axial posterior disc distraction: an experimental study on the rabbit lumbar spine model, Eur. Spine J. 15 (5) (2006) 597–604.
[67] K. Sato, S. Kikuchi, T. Yonezawa, In vivo intradiscal pressure measurement in healthy individuals and in patients with ongoing back problems, Spine 24 (23) (1999) 2468.
[68] A.R. Meir, J.C. Fairbank, D.A. Jones, D.S. McNally, J.P. Urban, High pressures and asymmetrical stresses in the scoliotic disc in the absence of muscle loading, Scoliosis 2 (1) (2007) 4.